

1

1 Different frequencies and triggers of canyon filling and flushing events in 2 Nazaré Canyon, offshore Portugal

3

4 Joshua R. Allin^{1,2}, James E. Hunt¹, Peter J. Talling¹, Michael A. Clare¹, Ed Pope^{1,2}, Douglas G. Masson¹5 ¹National Oceanography Centre Southampton, European Way, Southampton, SO14 3ZH, UK6 ²University of Southampton, Waterfront Campus, European Way, SO14 3ZH, UK

7 Corresponding author: J. R. Allin (jra1g13@soton.ac.uk)

8

Abstract

9 Submarine canyons are one of the most important pathways for sediment transport into ocean
10 basins. For this reason, understanding canyon architecture and sedimentary processes has
11 importance for sediment budgets, carbon cycling, and geohazard assessment. Despite increasing
12 knowledge of turbidity current triggers, the down-canyon variability in turbidity current frequency
13 within most canyon systems is not well constrained. New AMS radiocarbon chronologies from
14 canyon sediment cores illustrate significant variability in turbidity current frequency within Nazaré
15 Canyon through time. Generalised linear models and Cox proportional hazards models indicate a
16 strong influence of global sea level on the frequency of turbidity currents within the canyon.
17 Radiocarbon chronologies from basin sediment cores indicate that larger, canyon-flushing turbidity
18 currents reaching the Iberian Abyssal Plain have a significantly longer average recurrence interval
19 than turbidity currents that fill the canyon. The recurrence intervals of these larger turbidity currents
20 also appear to be unaffected by long-term changes in global sea level. This indicates that the factors
21 triggering, and thus controlling, the frequency of canyon-flushing and canyon-filling events are very
22 different. Canyon-filling appears to be predominantly controlled by sediment instability during sea
23 level lowstand and by storm and nepheloid transport during the present day highstand. Canyon-
24 flushing exhibits time-independent behaviour. This indicates that a temporally random process, or
25 summation of non-random processes that cannot be discerned from a random signal, are triggering
26 canyon flushing events.

1

27

28 **1 Introduction**

29

30 Understanding variability in turbidity current frequency and magnitude is important for several
31 reasons. First, turbidity currents are one of the most voluminous sediment transport mechanisms,
32 and they create some of the largest sediment accumulations on our planet (Ingersoll et al., 2003).
33 Second, understanding the frequency and scale of large turbidity currents informs risk assessment
34 for undersea installations that are at risk of damage by turbidity currents, such as oil and gas
35 infrastructure, pipelines, and telecommunications cables (Bruschi et al., 2006; Carter et al., 2012;
36 Carter et al., 2014).

37

38 Submarine canyon systems are recessed topographic features on continental margin slopes that act
39 as conduits for sediment transport into the deep sea (Stow et al., 1985; Normark and Piper, 1991;
40 van Weering et al., 2002). Turbidity currents are one of the main transport processes within
41 submarine canyon systems, and can be triggered by a wide variety of mechanisms. Potential triggers
42 include storm activity, tidal resuspension, sediment failures (triggered in some cases by
43 earthquakes), and river discharges (Marshall, 1978; Masson et al., 2006; Piper and Normark, 2009;
44 Masson et al., 2011a; Talling et al., 2012; Talling, 2014).

45

46 Turbidity currents in submarine canyons are proposed to be one of two broad end-member types:
47 filling and flushing (Parker, 1982; Piper and Savoye, 1993; Canals et al., 2006; Piper and Normark,
48 2009; Talling et al., 2012). Canyon-filling turbidity currents are hypothesised to slowly deposit
49 sediment within canyons over hundreds or even thousands of years (Paull et al., 2005; Canals et al.,
50 2006; Arzola et al., 2008; Puig, et al., 2014). Canyon-filling turbidity currents are considered to be the
51 result of localised sediment failures, hyperpycnal flows, or storm resuspension (Marshall, 1978;
52 Arzola et al., 2008; Khripounoff et al., 2009; Masson et al., 2011a; Talling et al., 2013; Talling, 2014).

53 Canyon-flushing turbidity currents are erosive flows that remobilise and transport large volumes of
54 this canyon-filling sediment out onto canyon-mouth fans or distal basin floors (Parker, 1982; Piper
55 and Savoye, 1993; Xu et al., 2004; Paull et al., 2005; Piper and Normark, 2009; Kriphounoff et al.,
56 2012; Talling et al., 2012; Puig et al., 2014). Canyon-flushing turbidity currents have yet to be directly
57 monitored, and are suggested to operate on much longer timescales than those that fill the canyon
58 (Piper and Savoye, 1993; de Stigter et al., 2007; Arzola et al., 2008; Talling et al., 2013). The causes of
59 canyon-flushing events are not clear, although they likely result from large sediment failures
60 (Normark and Piper, 1991; Masson et al., 2006; Goldfinger et al., 2007; Piper and Normark, 2009;
61 Hunt et al., 2013a; Talling, 2014).

62

63 **1.1 Observations of canyon-filling**

64

65 Previous work on the Nazaré Canyon has focussed on the factors controlling sedimentation within
66 the upper and middle reaches of the canyon (van Weering et al., 2002; de Stigter et al., 2007;
67 Oliveira et al., 2007; Arzola et al., 2008; Martin et al. 2011). As many as four turbidity currents have
68 been observed in the upper canyon per year (de Stigter et al., 2007; Martin et al., 2011; Masson et
69 al., 2011a). These frequent turbidity currents are typically the result of winter storms that re-
70 suspend canyon sediments, but may also be the result of small intra-canyon failures (de Stigter et al.,
71 2007; Martin et al., 2011; Masson et al., 2011a). Direct monitoring from below 4,000 m water depth
72 indicates that turbidity currents annually reach the lower canyon. However, these flows are generally
73 dilute, restricted to the incised thalweg, and are not considered to be erosive (de Stigter et al., 2007).

74

75 Canyon terraces at 3500 m water depth and 40 m elevation above the thalweg) record multiple
76 thicker (>25cm) turbidites deposited over the last 1,000 years. Turbidites recorded on terraces are
77 interpreted as the result of large flushing events by Arzola et al. (2008) and Masson et al. (2011a).
78 Given the presence of erosive scours within the lower reaches of the canyon, it is possible that these
79 frequent turbidity currents are erosive and flush sediment onto the canyon-mouth fan (Arzola et al.,

80 2008). To date, no deep water (>5000 m) core descriptions have been published from Nazaré
81 Canyon, and so our understanding of the recurrence rates of both canyon-filling and canyon-flushing
82 turbidity currents is limited to the upper and middle canyon, above 4,000 m water depth.

83

84 **1.2 Aims of the study**

85

86 Recent statistical analyses of long-term (>0.15 Ma) records indicates that large volume turbidites in
87 distal basin plains can have a temporally random distribution, and are not strongly influenced by
88 non-random glacio-eustatic sea level variability (Hunt et al., 2013a; Clare et al., 2014). Other studies
89 suggest that sea level is a dominant control; however, they do not consider a sufficient number of
90 events for statistical analysis (Maslin et al., 2004; Owen et al., 2007; Lee, 2009; Smith et al., 2013). It
91 has also been proposed that climate-driven sea level change can affect the frequency of canyon-
92 filling turbidity currents by influencing slope stability (Vail et al., 1977; Shanmugam and Moinola,
93 1982; Lebreiro et al., 1997; Piper and Normark, 2001; Lebreiro et al., 2009; Brothers et al., 2013).
94 Therefore, we first aim to determine whether the frequency of canyon-filling shows a significant
95 correlation with glacio-eustatic sea level change.

96

97 This present study is novel because few papers provide a complete overview of the frequency of
98 turbidity currents from the upper to lower reaches of submarine canyons and out into deep water
99 basins. No studies to date have statistically assessed both a basin and canyon record from a single
100 system to test for any overarching control on the recurrences of canyon-filling and canyon-flushing.
101 Therefore, also aim to assess whether or not canyon-flushing events have similar recurrence
102 intervals to canyon filling events, and whether their recurrence intervals have similar statistical
103 distributions. This will help determine whether they are likely to have similar (or different) triggers
104 (Urlaub et al., 2013; Clare et al., 2014; 2015).

105

106 **2 Regional setting**

107

108 The study area is located on the Western Iberian Margin between 36° and 43° N (Fig. 1). The shelf
109 and continental slope is incised by several large submarine canyons, including the Setúbal-Lisbon,
110 Cascais, Sao Vicente and Nazaré canyons. These canyons feed into 3 deep sedimentary basins; the
111 Iberian, Tagus and Horseshoe Abyssal Plains (Fig. 1).

112

113 **2.1 Nazaré Canyon**

114

115 Nazaré Canyon occurs in the central-west Iberian margin, and extends from ~1 km offshore from the
116 coastline and into the Iberian Abyssal Plain (Fig. 1). The canyon incision into the continental shelf and
117 slope coincides with the presence of the Nazaré Fault, which runs ENE-WSW and extends across the
118 margin. The Nazaré Canyon system is not directly fed by major rivers, as is the case with the Setúbal
119 and Cascais Canyons to the south. Instead, Nazaré Canyon is fed largely by littoral drift sediment
120 from smaller river systems to the north, and nepheloid transport of material to deeper sections of
121 the canyon (van Weering et al., 2002; Oliveira et al., 2007; de Stigter et al., 2007).

122

123 The canyon itself can be divided into three sections; the upper section that extends from the canyon
124 head to 2,000 m water depth; the middle section that spans between 2,000 and 4,000 m; and the
125 lower section that lies below 4,000 m (Figs. 2 and 3) (Vannev and Mougénot, 1990; van Weering et
126 al., 2002). The upper and middle sections have a steep v-shaped profile and are incised deeply into
127 the continental shelf (200 - 2,500 m water depth), with a channel thalweg that is <100 m wide. Below
128 4,000 m water depth the canyon broadens to a width of 8 – 10 km and is markedly less incised into
129 the substrate. Below 4,500 m water depth the canyon is less incised, and large levee structures have
130 developed to the north and south of the canyon axis. These levees are between 100 and 200 m in
131 height and taper distally into the Iberian Abyssal Plain, where they terminate at 5,300 m water depth
132 (Arzola et al., 2008; Lastras et al., 2009).

133

134 **2.2 Iberian Abyssal Plain**

135

136 The Iberian Abyssal Plain is located 200 km off the western coast of Portugal between 40° N and 43°
137 N and extends approximately 700 km to the northwest. The basin plain has an average water depth
138 of ~5,300 m but can be as deep as 5,400 m. The basin is bounded by the Galicia Bank to the
139 northeast, the Estremadura Spur to the south, and by a series of seamounts along its western
140 margin. The total area of the basin covers approximately 107,000 km². Previous work from ODP leg
141 149 has detailed the long-term basin infill record extending back to the Lower Cretaceous (140 Ma)
142 (Milkert et al., 1996a; 1996b). This work demonstrated an onset of, terrestrial-derived turbidite
143 deposition in the Iberian Abyssal Plain between 2.2 and 2.6 Ma, which continued into the late
144 Pleistocene. Despite the extensive record from ODP drilling legs in the Iberian Abyssal Plain, very
145 little of the recent (<100 ka) sedimentary architecture has been evaluated in detail. As a result, little
146 is currently known about the frequency of large volume turbidity currents in the basin through the
147 late Pleistocene.

148

149 **3 Materials and methods**

150

151 **3.1 Piston coring**

152

153 The cores used in this study have been collected by two different scientific campaigns. Piston cores
154 JC27-51, JC27-47 and JC27-46 come from the abyssal plain and levee sections, and were recovered
155 during cruise JC027. Core JC27-51 was retrieved from the Iberian Abyssal Plain, and cores JC27-46
156 and JC27-47 were retrieved from the northern external and internal levees respectively (Fig. 3). The
157 piston cores from the middle section of Nazaré Canyon were retrieved during cruise CD157. Cores
158 were sited using bathymetric and geophysical data. Cores D15738 and D15739 were both collected
159 from terraces 40 - 60 m above the canyon axis and have existing radiocarbon dates (Figs. 2 and 3).

160 There are no sediment cores from the upper canyon above 2,000 m water depth from which AMS
161 radiocarbon ages could be determined. The coarse-grained nature of the sediment in the upper
162 canyon, the rapid rate of accumulation, and the tidally-driven re-working of material prevent any
163 long-term record of turbidity currents being obtained through piston or gravity coring techniques (de
164 Stigter et al., 2007).

165

166 **3.2 Identification of turbidites and hemipelagite**

167

168 In order to develop age models and determine recurrence intervals for turbidity currents,
169 differentiating their deposits from background hemipelagic sediment is vital. Hemipelagic sediments
170 typically contain randomly dispersed foraminifera giving a pitted surface texture. They also lack
171 primary sedimentary structures and are often bioturbated (Stow and Piper, 1984). In contrast,
172 turbidity current deposits are often well sorted, have normal grading, and have observable internal
173 structure. The fine-grained mud cap of turbidity currents is commonly homogenous and often devoid
174 of foraminiferal material, while the basal contact of turbidites is often sharp and sometimes
175 erosional (Bouma, 1962; Stow and Piper, 1984).

176

177 Cores were logged for sedimentary features such as grain size, sedimentary structures and colour.
178 The cores were logged using a GeotekTM multi-sensor core logger (MSCL) for petrophysical data,
179 particularly optical lightness and spectral reflectance. ITRAX-XRF geochemical data were obtained for
180 JC27-51 to aid in the construction of the age-model using hemipelagic sediment. It has been shown
181 that hemipelagic sediment in basin settings has a chemistry that is distinct from terrestrially-derived
182 siliciclastic sediment, primarily due to a high proportion of detrital carbonate (Croudace et al., 2006).
183 Where ITRAX-XRF data were not available, optical lightness (L^*) was used to discriminate between
184 Turbidite and hemipelagic deposits. High amounts of foraminiferal carbonate in basin sediments
185 result in a lighter colour than terrestrially derived mass-flow deposits (Balsam et al., 1999).

186

187 3.3 Age model development

188

189 Age control for this study is provided by AMS radiocarbon dating. AMS radiocarbon dates were
190 obtained for cores JC27-51, JC27-47 and JC27-46 in order to develop age models and calculate
191 turbidity current recurrence intervals. Nine AMS radiocarbon dates were previously determined for
192 terrace cores D15738 and D15739 (Masson et al., 2010) (Table 1). Samples were taken from
193 hemipelagic mud units, with care being taken to avoid sampling any turbidite mud or coarse
194 turbidite bases. In cores JC27-51, JC27-47 and JC27-46, 2 - 10 cm³ of sediment was sampled to pick
195 the 8 - 10 mg of foraminifera required for accurate AMS 14C dates. No one foraminiferal species was
196 abundant enough to collect monospecific samples in all cases, so most samples consist of mixed
197 species assemblages. The dominant species were *Orbulina universa*, *Globigerina bulloides*,
198 *Neogloboquadrina pachyderma*, *Globorotalia truncatulinoides*, *Globigerinoides ruber* and
199 *Globorotalia hirsute*. Where monospecific samples were possible, *Orbulina universa* was selected.
200 The conventional radiocarbon ages returned from analysis were converted to calibrated ages (Cal
201 years BP) using the MARINE13 database (Reimer et al., 2013) (Table 1).

202

203 In order to account for local reservoir offsets, an average of five reservoir correction (ΔR) values was
204 used from nearby locations. These ΔR values are from samples collected along the Iberian shelf; the
205 main pathway for ocean currents and sediment transport to the head of Nazaré Canyon (Monges
206 Soares, 1993; van Weering et al., 2002; Oliveira et al., 2007; de Stigter et al., 2007). This yields a ΔR
207 correction value of +267 years, which is consistent with reconstructed past reservoir offsets along
208 the Iberian Margin (Bronk Ramsey et al., 2012).

209

210 Using the radiocarbon ages, and the thicknesses of hemipelagic sediment between them,
211 sedimentation rates were calculated. The thicknesses of hemipelagic sediment were then divided by
212 the sedimentation rates to convert them into time intervals (Wynn et al., 2002; Grácia et al., 2010;
213 Clare et al., 2014). From these time intervals the ages of individual turbidites can be estimated (Table

214 2; Suppl. info.). This method relies on the assumption that there is minimal fluctuation in the rate of
215 hemipelagic sediment accumulation through time (Lebreiro et al., 2009; Grácia *et al*, 2010; Clare et
216 al., 2015). It also relies on the assumption that subsequent turbidity currents are not significantly
217 erosive (Weaver and Thomson, 1993; Thomson and Weaver, 1994; Weaver, 1994; Wynn et al., 2002;
218 Gutiérrez-Pastor et al., 2009; Grácia et al., 2010).

219

220 **3.4 Calculation of turbidite recurrence intervals and frequency**

221

222 Using the age model to estimate the emplacement age of each turbidite allows us to calculate
223 individual recurrence intervals. Here we define the recurrence interval of a turbidite as the length of
224 time since the turbidite that preceded it (Clare et al., 2014; 2015; Pope et al., 2015). Where
225 hemipelagic age models cannot be constructed, we calculate recurrence interval by dividing the length
226 of time by the number of turbidites to get an 'average recurrence interval'. The determination of
227 recurrence intervals requires that individual turbidites be distinguished from multiple upward-fining
228 units deposited during the same turbidity current. These multiples of upward-fining sediment can
229 result from differential sorting due to changing bed-shear stresses, or from multi-staged failures.
230 (Piper and Bowen, 1978; Stow and Shanmugam, 1980; Hunt et al., 2013b). Interpreting multiple
231 upward-fining units within a single turbidite as multiple individual turbidites has the potential to bias
232 any analysis by the incorrect counting of turbidites; and hence, incorrectly estimating their
233 recurrence intervals (Lebreiro et al., 2009).

234

235 **3.5 Statistical analysis of turbidite recurrence and frequency**

236

237 Statistical analysis can be a powerful tool for the analysis of time series data, such as turbidite
238 recurrence (e.g. Hunt et al., 2014; Moernaut et al., 2015; Ratzov et al., 2015); however, it is
239 important to understand how recurrence is measured before specific tests are selected. Recurrence

240 is here inferred from intervals of hemipelagic fallout between turbidity currents, and the average
241 accumulation rate of hemipelagic mud between dated horizons. This method is most appropriate in
242 distal basin settings, such as basin core JC27-51 where past work has shown there is little or no
243 erosion by successive turbidity current, and the hemipelagic mud is not removed (Weaver and
244 Thomson, 1993; Thomson and Weaver, 1994; Weaver, 1994; Wynn et al., 2002; Gutiérrez-Pastor et
245 al., 2009; Grácia et al., 2010; Clare et al., 2014). In more proximal, slope and confined settings, the
246 effects of erosion may be greater, but it is difficult to discern this from core samples due to their
247 relatively narrow diameter (typically 10 cm). We therefore bin the data at the more proximal levee
248 core site JC27-46, by counting the number of turbidites within prescribed time intervals to account
249 for this uncertainty in the precise measurement of individual recurrence intervals. As bin dimensions
250 can potentially affect the statistical outcome (Urlaub et al., 2013; Pope et al., 2015) we consider
251 three different bin widths (250, 500 and 1000 years) in our analysis. We investigate the influence of
252 sea level on binned turbidite recurrence at levee site JC27-46, where sufficient turbidites were
253 sampled (N=201) to permit regression and survival analysis. In addition to different data bin sizes, we
254 also use three different sea level curves as our explanatory variable. The sea level reconstructions of
255 Lambeck et al. (2014), Rohling et al. (2010), and Peltier and Fairbanks (2006) are widely used and
256 have suitable resolution over the late Pleistocene. Less sophisticated frequency analysis is used for
257 individual turbidite recurrence intervals at basin site JC27-51, as fewer turbidites were sampled
258 (N=26) thus limiting the power of statistical tests (Pope et al., 2015).

259

260 ***3.5.1 Assessing the significance of sea level on turbidite recurrence at JC27-46***

261

262 We use two different statistical analyses to investigate the significance of sea level in relation to
263 turbidite recurrence at JC27-46. The first is a parametric Generalised Linear Model, which tests for
264 the significance of sea level as an explanatory variable on the recurrence of turbidites (McCullagh
265 and Nelder, 1989; Clare et al., 2016). As it is a parametric test, the Generalised Linear Model requires
266 *a priori* definition of the distribution form of the relationship between the two variables. We apply

267 variants of the model using Gamma, Gaussian and Poisson distribution forms, and assess the most
268 appropriate model using quantile-quantile (Q-Q) plots. While Q-Q plots do not provide a quantitative
269 measure of the goodness-of-fit, they can be qualitatively interpreted to understand how much a
270 given data set deviates from the specified distribution (Salkind and Rasmussen, 2007).

271

272 General rules of thumb exist for determining the minimum sample size for regression analysis.
273 Tabachnick and Fidell (2007) indicate that testing for the effect of one individual variable will require
274 $N=106$ events. Green (1991) performed a more detailed analysis, which incorporated an assessment
275 of statistical power and effect size, suggesting that at least $N=23$ is required to detect large effects
276 and $N=53$ for detecting medium effects of one explanatory variable. We also apply a non-parametric
277 Cox Proportional Hazards (PH) Model (Cox, 1972) as a comparative test because it requires no *a*
278 *priori* specification of frequency distribution form. The Cox PH model is typically used to determine a
279 hazard rate in medical studies (e.g. rate of patient fatality) but has also been applied to turbidite
280 frequency analysis (Hunt et al., 2014; Clare et al., 2016). The hazard rate is the ratio between the
281 change in the explanatory variable (e.g. sea level) and the response variable – in this case turbidite
282 recurrence. Previous work has shown that the Cox PH model requires at least a minimum sample size
283 of $N=20$ (Vittinghoff and McCulloch, 2007). The Cox PH model performs survival analysis and three
284 separate tests (likelihood, Wald and log-rank), for which a p-value is derived. For both Generalised
285 linear and Cox PH models, where the resultant p-value is small (<0.05) sea level is found to be a
286 significant variable to explain turbidite recurrence. Where the p-value is large ($p>0.05$), sea level
287 cannot be implicated as a statistically significant control on turbidite recurrence. Levee core site
288 JC27-46 features $N=201$ turbidites, which is well above the minimum sample size threshold for both
289 regression and survival analysis. Distal basin core JC27-51 only features $N=26$ turbidites, which is at
290 the minimum sample size limit, and therefore would yield only low statistical power. Therefore, we
291 simply analyse the frequency distribution form of turbidite recurrence at JC27-51 to provide insights
292 into triggering and possible controls, instead of performing more sophisticated survival or regression
293 analysis.

294

295 **3.5.2 What is the frequency distribution form of turbidite recurrence at JC27-51?**

296

297 A Poisson distribution implies time-independence and a lack of memory in a system (Parzen, 1962).

298 Thus, recurrence intervals that fit a Poisson (exponential) distribution form can be viewed as

299 occurring randomly in time, with no dependence on when the previous event occurred, or when the

300 next will happen. This memoryless, time-independent behaviour is in contrast to non-random

301 processes such as sea level change. Therefore, where recurrence intervals conform to a Poisson

302 distribution, non-random processes cannot be directly attributed to a singular or dominant control

303 on recurrence (Urlaub et al., 2013; Clare et al., 2014). In contrast, time-dependent distributions may

304 indicate that a single process (e.g. Normal) or series of processes (e.g. log-normal) are exerting

305 significant control on a system (van Rooij et al., 2013; Clare et al., 2016). Therefore, we aim to

306 determine the frequency distribution form of turbidite recurrence intervals at JC27-51 to provide

307 some insights into possible triggering and controlling mechanisms for canyon flushing events. We

308 also aim to determine whether the frequency distribution form of turbidite recurrence at the basin

309 plain is distinctly different to that observed at the more proximal levee location.

310

311 Here we employ parametric and non-parametric goodness-of-fit methods to test recurrence interval

312 distribution. The Anderson-Darling test is a parametric test that tells us the probabilities that the

313 data come from different populations with specific distributions, including Poisson, normal, log-

314 normal and Weibull (Stephens, 1974). To further test the distribution of canyon flushing events, we

315 use non-parametric (Mann-Whitney and Kolmogorov-Smirnov) tests to determine if the frequency

316 distribution form of Iberian Basin turbidite recurrence is significantly different to that of other distal

317 basin plains. For this, we use the published dataset of Clare et al. (2014; 2015), which demonstrates

318 that multiple basin turbidite records conform to a Poisson distribution. The Mann-Whitney test is

319 based on the null hypothesis that the datasets are sampled from populations with identical

320 distributions (Lehmann and D'Abrera, 2006). The Kolmogorov-Smirnov test compares the cumulative

321 distributions of two data sets and poses the null hypothesis that they were randomly sampled from
322 populations with identical frequency distributions (Lehmann and D'Abrera, 2006). The result tells us
323 the probability that the two cumulative frequency distributions would be as far apart as observed in
324 our data. We use these three tests to provide confidence in our results.

325

326 **4 Results**

327

328 **4.1 Core sedimentary characteristics**

329

330 Core JC27-51 shows a depositional sequence comprised of pale grey mud units with abundant
331 foraminifera interbedded with well sorted and normally-graded sedimentary units (Fig. 3). The
332 graded units are often greater than 50 cm thick and many are mud-dominated (Fig. 4A). Some of
333 these mud-dominated deposits exhibit thin silt or fine sand bases. Three deposits within the core
334 have sandy bases, with one of these (core depth 320 - 390 cm) having a much thicker medium- to
335 coarse-grained sand base with planar and ripple laminations (Fig. 4B). We interpret these graded
336 units as turbidite deposits after Bouma (1962), and Stow and Piper (1984). A silt unit with
337 interspersed mud clasts occurs at 395 - 420 cm depth in the core, and has a subtle reverse-to-
338 normally graded sequence (Fig. 4C), which we interpret as a debrite, in the sense of Naylor (1980).

339

340 The pale sediment in core JC27-51 exhibits different colour, grain size, and lightness characteristics
341 than turbidite deposits (Fig. 5A). Unlike the more homogenous olive-green turbidites, the pale grey
342 sediment is noticeably rich in foraminiferal sand and exhibits bioturbation structures. This
343 foraminiferal sand gives the sediment a pitted surface texture. From the photospectrometer data the
344 pale grey sediment in JC27-51 exhibits an L* value typically within a range of 50 - 65, while turbidites
345 are typically within 35 - 50. From the ITRAX XRF Calcium counts (kcps) data, the pale grey sediment
346 typically exhibits values greater than 160 kcps (Fig. 5A). In contrast, turbidite deposits have values

347 ranging from 40 to 120 kcps. These differences in the geochemical and geophysical properties are
348 likely due to the high amounts of calcareous foraminiferal shells within the sediment. We interpret
349 this pale grey sediment as background hemipelagic accumulation, after Stow and Piper (1984) and
350 Hoogakker et al. (2004). Typically, the boundaries between the upper turbidite mud cap and the
351 following hemipelagic sediment are gradational (Fig. 5A). This is due largely to bioturbation, but also
352 likely due to the slow settling of turbidite mud suspension clouds and incorporation of carbonate
353 material from background hemipelagic sediment. The boundaries between the bases of the turbidite
354 deposits are flat and sharp (Fig. 5A).

355

356 Core JC27-46 consists largely of interbedded silt and fine sand units that are normally graded and
357 typically have thin mud caps (Fig 4). These graded deposits can be broadly classified into two
358 different types. Type 1 deposits are normally graded, with 1 - 4 cm thick silt or fine sand bases, and
359 thicker 10 - 20 cm upper mud units. Type 2 deposits are thinly-bedded and have 0.5 - 4 cm thick,
360 faintly gradational fine- to medium-grained sand bases. The thin sand bases typically grade sharply
361 into a thin (0.5 - 3 cm) fine-grained mud (Fig. 4D and E). Type 1 deposits are dominant in the upper 6
362 m of the core, while type 2 are dominant in the lower 4 m. We interpret these deposits to be the
363 result of turbidity currents in the sense of Stow and Shanmugam (1980). Within the core there are
364 lighter, pale grey units that are rich in foraminiferal sand, have a pitted surface, and show evidence
365 of bioturbation. Based on the similarity with hemipelagic deposits from core JC27-51 we also
366 interpret these to have a hemipelagic origin.

367

368 Core JC27-47 is dominated by thicker sand-rich, normally-graded deposits with medium- to coarse-
369 grained sand bases (Fig. 4F and G). Sand units vary between 0.5 and 20 cm thick and grade sharply
370 into fine-grained mud. Several of these deposits have clear erosional bases, with several units
371 presenting a chaotic texture and uneven or folded bedding (Fig. 4G). We interpret deposits with
372 normal grading and erosional bases to be turbidites (Fig. 4F). Deposits with folded bedding or chaotic
373 texture are interpreted to be the result of small-scale slumping or debris flows after Shanmugam et

374 al. (1995). The upper 60 cm of the core contains of the same pale grey, bioturbated and
375 foraminiferal-rich sediment present in cores JC27-46 and JC27-51. As with the two previous cores,
376 we interpret this to be hemipelagic sediment. Hemipelagic sediment is not present below 60 cm
377 depth in the core, possibly due to erosion from subsequent turbidites over-spilling the internal
378 canyon levee (Fig. 3).

379

380 Middle canyon cores are located on terraces at 40 - 60 m elevation above the canyon thalweg (Fig.
381 3). Cores D15738 and D15739 are composed largely of clay with interspersed faintly-graded fine sand
382 or silt beds (Fig. 3). These are interpreted by Arzola et al. (2008) as turbidite deposits resulting from
383 turbidity currents that overspill onto canyon terraces. Basal contacts between the sand and the
384 underlying mud are typically erosional, and previous work indicates there is no discernible
385 hemipelagic material between turbidite units due to the high level of shelf-derived terrigenous
386 material transported in nepheloid layers to deeper in the canyon (de Stigter et al., 2007; Arzola et al.,
387 2008).

388

389 **4.2 Age model and sedimentation rate**

390

391 Seven AMS radiocarbon dates were collected from JC27-51, five from JC27-46 and five from JC27-47
392 (Fig. 3). Using these dates and the known thickness of hemipelagic sedimentation, age models place
393 the base of core JC27-51 at ca 83,000 Cal years BP and the base of core JC27-46 at ca 33,500 Cal
394 years BP (Fig. 6). Linear regressions on the age models yielded R^2 values of 0.9934 and 0.9975 in
395 cores JC27-51 and JC27-46 respectively (Fig. 6). These values give us a high level of certainty in a
396 stable hemipelagic sedimentation rate over long periods at both core sites (Swan and Sandilands,
397 1995). Average hemipelagic sedimentation rates for cores JC27-51 and JC27-46 are 2.3 and 7.8 cm/ka
398 respectively (Fig. 6).

399

400 Individual turbidite ages derived from the two age models can be seen in Table 2, and in
401 Supplementary Table 1. Due to the presence of multiple erosive sandy turbidites in core JC27-47,
402 hemipelagic material is only discernible in the upper 60 cm (Fig. 3). Below 60 cm core depth,
403 hemipelagic sediment is sparse and indistinguishable from fine-grained turbidite deposits. Similarly
404 in cores D15738 and D15739, hemipelagic deposits contain a high percentage of terrigenous mud
405 with sparse foraminifera, and are therefore indistinguishable from turbidite muds (Arzola et al.,
406 2008; Masson et al., 2011a). AMS radiocarbon dates from cores JC27-47, D15738 and D15739
407 originate from foraminifera collected out of bulk sediment samples. Because of the uncertainty in
408 correctly defining hemipelagic thicknesses, recurrence intervals for each deposit cannot be
409 calculated using a hemipelagic age model. Instead, an average turbidity current recurrence interval is
410 calculated by dividing the number of turbidites by the time between radiocarbon dates (Fig. 3).

411

412 **4.3 Regular filling events in the middle canyon**

413

414 Previously collected AMS radiocarbon ages from middle canyon terrace cores place the bases of
415 cores D15738 and D15739 at ca 1,500 BP and ca 1,000 BP respectively. Core D15738 contains 25
416 identifiable sandy turbidite bases above the oldest AMS radiocarbon date, while core D15739 has 21
417 turbidites above the oldest radiocarbon date (Fig. 3). By dividing the time interval by the number of
418 turbidites we are able to calculate an average recurrence for turbidites. This gives us give an average
419 turbidity current recurrence of 43 years on terraces that are 40 - 60 m above the canyon floor.

420

421 **4.4 Sea level control on canyon-filling in JC27-46**

422

423 For visual comparison of sea level and turbidite frequency, we use the 500 year binned turbidite data
424 from core JC27-46 (Fig. 7A). This 500 year interval is considered to be an appropriate resolution for
425 the length of the record (Lebreiro et al., 2009). Turbidite frequency in core JC27-46 on the external
426 levee crest is highly variable during the sea level lowstand from 33.5 to 23.5 ka; the 10,000 year

427 period prior to North Atlantic warming and associated sea level rise (Clark et al., 2004; Anders and
428 Carlson, 2012) (Fig. 7A). From the modelled ages for turbidites, an average of the estimated
429 recurrence intervals during lowstand conditions is 68 years, lower than at any point during the
430 33,500 year record.

431

432 Turbidite frequency decreased to 0 – 3 events per 500 years during the period from 23 and 19.5 ka,
433 the onset of sea level transgression (Fig. 7A). This initial decline of turbidite frequency starting at 23
434 ka occurred considerably before the rapid global eustatic sea level rise at 20 ka (Chappelle, 2002;
435 Peltier and Fairbanks, 2006; Clark et al., 2009; Rohling et al., 2009; Lambeck et al., 2014). Following
436 the onset of rapid sea level rise at 17 - 19 ka (Clark et al., 2004; 2009), there is an increase in
437 frequency (4 turbidites/500 years) that lasts until 15.5 ka. Turbidite frequency decreased significantly
438 after 15 ka towards the Younger Dryas. An average of recurrence intervals for the global sea level
439 transgression is 300 years. Following the onset of the present-day sea level highstand at ~7 ka there
440 is an average of recurrence intervals of 1625 years (Fig. 7A).

441

442 A similar pattern of increasing recurrence intervals through the period of deglaciation can be seen in
443 JC27-47 (Fig. 7B). The recurrence interval values for turbidites are also broadly comparable to those
444 recorded in JC27-46 on the external levee for the same time period. In JC27-47, recurrence intervals
445 are approximately 120 years at the beginning of sea level transgression at 20 ka. During the end of
446 the sea level transgression the average recurrence interval increases to 320 years, similar to the 300
447 year recurrence rate found in JC27-46 (Fig. 7A and B). As in core JC27-46, following the onset of the
448 present-day highstand at 7 ka, recurrence intervals have increased to >1000 years (Fig. 7B).

449

450 The results of generalised linear models indicate that sea level is a significant explanatory variable
451 ($p < 0.05$; Supplementary table 2) in relation to the frequency of late Pleistocene canyon-filling
452 turbidity currents at JC27-46. As observed visually, periods of lowered sea level correspond to more
453 frequent turbidity currents. This correlation holds for individual and binned (250, 500 and 1000 year)

454 recurrence intervals, against all of the sea level curves that are considered by this study (i.e. (Rohling
455 et al., 2010; Peltier and Fairbanks, 2006; Lambeck et al., 2014; Suppl. Table 2). A Gaussian
456 distribution appears to best parameterise the relationship. Cox Proportional Hazard Models also
457 indicate a significant influence of sea level on the turbidite recurrence for all but two model runs; a
458 significant relationship was not observed when the Lambeck et al. (2014) sea level curve is analysed
459 against 250 year-bins and individual turbidite recurrence (Suppl. table 2).

460

461 **4.5 Time-independent canyon-flushing in JC27-51**

462

463 The most recent turbidite present in core JC27-51 from the Iberian Abyssal Plain dates to ca 4,850
464 Cal years BP, while the oldest dates to ca 82,000 Cal years BP (Table 2). Based on a hemipelagic
465 sedimentation rate of 2.3 cm/ka (Fig. 6) a lack of hemipelagite between two turbidites indicates a
466 short recurrence interval. Turbidity currents in the basin are assumed to be non-erosive, and so two
467 or more turbidites with no intervening hemipelagite are assumed to be near-synchronous, and are
468 assigned a recurrence interval of 0 years (Table 2). This gives a 2,880 year average of recurrence
469 intervals for flushing turbidity currents that reach the Iberian Abyssal Plain.

470

471 We compare the recurrence intervals for JC27-51 with data from four other distal basin plains (Clare
472 et al., 2014; 2015). When recurrence intervals are normalised to the mean value for each dataset,
473 they all fit an approximately straight line fit on an exceedance plot (Fig. 8), which is indicative of an
474 exponential distribution. Non-parametric Mann-Whitney and Kolmogorov-Smirnov tests
475 demonstrate statistically that the distribution form of turbidite recurrence at JC27-51 shows no
476 significant difference to the four other exponentially-distributed basin plain records (Supplementary
477 Table 3). Given the relatively small sample size (i.e. N=26), it is possible that we do not have
478 sufficient turbidites to make a fully conclusive statement, but we can state that it is not possible to
479 differentiate the recurrence record from other time-independent records. The Mann-Whitney and
480 Kolmogorov-Smirnov tests also allow us to demonstrate that the frequency distribution form of

481 turbidite recurrence in the basin plain (JC27-51) is significantly different ($p < 0.0001$) to the time-
482 dependent recurrence at levee location JC27-46. Thus, recurrence intervals for canyon-flushing
483 turbidites in the Iberian Abyssal Plain may be considered time-independent and occurring at a
484 significantly different tempo and to that of canyon-filling flows.

485

486 **5. Discussion**

487

488 In this section we first discuss the triggers and controls on canyon-filling turbidity currents in Nazaré
489 Canyon, and how external factors such as sea level affect recurrence rates. Second, we discuss the
490 possible triggering mechanisms for large canyon-flushing turbidity currents. Finally, we evaluate the
491 implications of these findings for geohazard assessment and in light of future climate change
492 predictions.

493

494 **5.1 Canyon-filling in the present day highstand**

495

496 The process of canyon-filling occurs on a variety of different temporal and spatial scales within
497 Nazaré Canyon. Previous monitoring in Nazaré Canyon has documented as many as four turbidity
498 currents may occur in the upper canyon per year (de Stigter et al., 2007; Martin et al., 2011; Masson
499 et al., 2011a). These small and frequent turbidity currents do not appear to deposit on canyon
500 levees, or the abyssal plain, as there is a general absence of turbidites deposited more recently than
501 3 ka (Figs 3, and 7A and B). These sub-annual turbidity currents are confined primarily to the incised
502 canyon thalweg and typically dissipate before reaching depths greater than 4,000 m water depth
503 (Fig. 9A). One turbidity current recorded by de Stigter et al. (2007) below 4,000 m water depth also
504 did not appear to deposit on canyon levees or on the abyssal plain. These flows may erode
505 previously emplaced sediment, but are not considered to flush large volumes of material (Fig. 9A).

506

507 Terrace cores at 3,500 m water depth and 40 m elevation above the thalweg reveal a mean
508 recurrence of 43 years for larger turbidity currents over the last 1,000 years. These distal turbidite
509 deposits are interpreted as the result of large flushing turbidity currents by Arzola *et al.* (2008),
510 although there is no evidence of post 1 ka deposits in the Iberian Abyssal Plain that would indicate
511 canyon-flushing has occurred (Fig. 4, and 7A and B). Given the presence of erosive scours within the
512 lower reaches of the canyon, it is possible that these frequent turbidity currents are erosive and do
513 flush sediment from for the upper to the lower canyon, but are too small to overtop levees or reach
514 the abyssal plain (Fig. 9A) (de Stigter *et al.*, 2002; Arzola *et al.*, 2008). However, no age-models exist
515 for lower canyon cores making this difficult to support.

516

517 **5.2 Canyon-filling during sea level lowstand**

518

519 The role of sea level lowstand in exposing continental shelves and resulting in more terrigenous
520 sediment delivery to slope and deep-sea fans is widely accepted; as is the role of canyons as conduits
521 for this sediment delivery (Vail *et al.*, 1977; Shanmugam and Moiola, 1982; Posamentier *et al.*, 1991;
522 Piper and Savoye, 1993; Lebreiro *et al.*, 1997; Clark and Mix, 2000; Ducassou *et al.*, 2009; Lebreiro *et al.*,
523 *et al.*, 2009; Covault and Graham, 2010). Our hemipelagic age model reveals that the frequency of
524 canyon-filling turbidity currents was highest during sea level lowstand (Fig. 7A and B). Lowstand-
525 dominated canyons typically occur when the canyon does not incise the entire continental shelf
526 (Covault and Graham, 2010). During highstand conditions such canyons are not in direct contact with
527 the shoreline or fluvial sources, limiting sediment delivery. During sea level lowstand, sequence
528 stratigraphic models predict direct connection between rivers and canyon heads. This results in a
529 higher frequency of turbidity currents due to increased sediment supply and associated instability
530 (Shanmugam and Moiola, 1982; Stow *et al.*, 1984; Posamentier *et al.*, 1991; Piper and Savoye, 1993;
531 Lebreiro *et al.*, 2009; Covault and Graham, 2010).

532

533 During sea level lowstand the larger area of exposed continental shelf likely resulted in greater
534 erosion and littoral sediment delivery to the Nazaré Canyon head (Fig. 9B) (Posamentier et al., 1991;
535 Sommerfield and Lee, 2004; Durán et al., 2013). Despite the lack of a direct fluvial sediment supply
536 into Nazaré Canyon, there are a number of small river systems to the north which feed onto the
537 continental shelf (Fig. 9B). Increased sediment supply to the shelf from these river systems during
538 lowstand conditions may also have led to increased littoral sediment transport, and contributed to
539 the higher frequency of turbidity currents being generated (Fig. 9B). It is also possible that these river
540 systems were routed across the shelf and into the canyon head during sea level lowstand, although
541 there is no geomorphic evidence available to support this.

542

543 Lebreiro et al. (2009) have suggested that slope instability in the Setúbal/Lisbon and Cascais Canyons
544 (Fig. 1) is highest during sea level transgression. This implies that large turbidity currents that fill the
545 Setúbal/Lisbon and Cascais Canyons switch-off at 15.5 ka. Work by Masson et al. (2011b) instead
546 demonstrates that the Setúbal/Lisbon and Cascais Canyons experience an almost complete switch-
547 off in large canyon-filling turbidity current activity at 6.6 ka. The switch-off of canyon-filling activity in
548 the Setúbal/Lisbon and Cascais Canyons proposed by Lebreiro et al. (2009) at 15.5 ka could more
549 easily be explained by the 200 m elevation of their core site. This elevation above the canyon would
550 bias the record towards the largest turbidity currents (de Stigter et al., 2011). Our age models and
551 statistical analyses from Nazaré Canyon also indicate that large canyon-filling turbidity currents
552 switch-off at ~7 ka (Fig. 9B). This is suggestive of a margin-wide sea level control on large-scale
553 canyon-filling in Portuguese Margin canyons.

554

555 ***5.2.1 Uncertainties of the statistical analyses***

556

557 The results of the generalised linear models and Cox proportional hazards models indicate that sea
558 level is well correlated with turbidite frequency recorded on the external canyon levee
559 (Supplementary table 2). While sea level is generally accepted as having a dominant control on

560 sedimentation in many other deep sea fan settings, our results should be treated with some caution.
561 Our data set contains 201 turbidites, and while this is a sufficient number for regression-based
562 analyses (Green, 1991; VanVoorhis and Morgan, 2007), it is smaller than many other datasets used in
563 statistical analyses of recurrence (Clare et al., 2014; 2015). The height of the JC27-46 core site above
564 the canyon floor may also bias the turbidite record towards those turbidity currents large enough to
565 over-spill the outer levee. There may also be turbidite deposits that are not visually detectable
566 because they are sub-millimetre in scale. Moreover, the sea level curves used in this study are all
567 global (eustatic) reconstructions, and may not be suitable for local analysis where the effect of
568 eustatic sea level changes may be outweighed or convoluted by localised isostatic and tectonic
569 influences (Shanmugam and Moiola, 1982; Stow et al., 1984; Covault and Graham, 2010; Romans et
570 al., 2015). Importantly, binning the data appears to have an effect on the significance of sea level.
571 500 year and 1000 year bin sizes appear to be less significant or not significant when tested against
572 sea level (Supplementary Table 2). This has also been observed in other statistical analyses of
573 turbidite recurrence (Urlaub et al., 2013; Pope et al., 2015)

574

575 **5.3 Potential triggers of canyon-flushing**

576

577 The frequency distribution of canyon flushing flows in Nazaré Canyon is indicative of temporally
578 random, time-independent behaviour. A temporally random distribution can result from *a)* a single
579 temporally random or pseudo-random process, *b)* numerous non-random processes affecting a
580 single source overprinting and resulting in a random distribution, *c)* several different sources feeding
581 into the same basin, or *d)* shredding of environmental (triggering) signal due to the long recurrence
582 intervals (Urlaub et al., 2013; van Rooij et al., 2013; Clare et al., 2014; 2015; Pope et al., 2015;
583 Romans et al., 2015). Here we will evaluate different processes that could trigger canyon-flushing
584 events.

585

586 **5.3.1 Are large storms a trigger?**

587

588 It has been stated that storms have the potential to trigger turbidity currents that transport sand
589 into deep water (TsuTsu et al., 1987; Shanmugam, 2008). Within Nazaré Canyon, storm-triggered
590 turbidity currents play a significant role in small-scale canyon-filling during the present day (Fig. 9A)
591 (van Weering et al., 2002; de Stigter et al., 2007; Martin et al., 2011; Masson et al., 2011a). One of
592 the limiting factors in assessing the role of storms in canyon-flushing events is the length of the
593 observational record. Meteorological data available for the last 63 years indicates that there have
594 been over 150 storms (wave height >1.6 m) recorded since 1952 (Lozano et al., 2004; Almeida et al.,
595 2011). Despite the number of storm events, we see no recent turbidite deposits in the levee or
596 abyssal plain cores; however, the cores may not contain the most recent sediments due to sampling
597 loss. If storms had been a trigger of canyon-flushing through the Holocene, we would expect to see
598 turbidites throughout Holocene sedimentary sequences. It may be possible that some extremely rare
599 storms are large enough to generate turbidity currents that are erosive and capable of flushing the
600 canyon. The lack of turbidites observed in the Iberian Abyssal Plain during last 2,000 years, combined
601 with the likely number of storm events, makes it improbable that storms are a trigger of canyon-
602 flushing (Fig. 3 and table 2).

603

604 ***5.3.2 Is sea level control undetectable due to 'signal shredding'?***

605

606 Certain sedimentary environments serve as ideal long-term archives of climatic or environmental
607 signals. This is particularly true in the case of deep-water fan and continental slope settings. In these
608 deep-water settings, one of the principal expressions of sea level variability is changes in down-
609 system sediment transport (Stow and Piper, 1984; Posamentier et al., 1991; Covault and Graham,
610 2010; Covault et al., 2010).

611

612 Signal shredding can be defined here as the filtration of environmental signals through a system by a
613 non-linear process; in this case sediment transport (Jerolmack and Paola, 2010; Romans et al., 2015).

614 Environmental signals like sea level may be considered a linear input into a system. However, the
615 recording of this signal in sedimentary archives by sediment transport and deposition is typically
616 non-linear. This is because sediment transport and deposition is highly variable and dependent on
617 several initial and transport conditions. For turbidity currents these can include the triggering
618 mechanism, sediment volume, run-out distance, and whether or not these currents bypass or
619 deposit (Piper and Normark, 2009; Talling et al., 2013, Talling, 2014). These preconditions impart
620 non-linearity that can ultimately filter or 'shred' the signal of environmental change. In the case of
621 Nazaré canyon-filling turbidity currents, the sea level signal is preserved in the levee due to the
622 number of events recorded, the proximity to source, and the regularity with which they were
623 deposited. The height of the levee above the canyon also likely prevents smaller, more frequent
624 events triggered by storm or wave activity from depositing at the core site. Storm and wave activity
625 could be considered a separate environmental signal and may mask the longer-term sea level signal
626 (Romans et al., 2015).

627

628 In contrast to this, canyon-flushing events are typically less frequent, often having recurrence
629 intervals of >2000 years (Fig. 9 and Table 2). They involve the remobilisation of sediment stored
630 within the canyon over many thousands of years (Paull et al., 2005; Talling et al., 2007; Piper and
631 Normark, 2009; Talling, 2014). This implies that if canyon-flushing events are the result of climatic
632 variability or change, their rarity (non-linearity) in the depositional record could have shredded any
633 signal of this climatic control (Covault and Fildani, 2014; Clare et al., 2015; Romans et al., 2015). Such
634 signal-shredding could explain the temporally random distribution of canyon-flushing events in the
635 Iberian Abyssal Plain.

636

637 ***5.3.3 Are regional earthquakes a trigger?***

638

639 Turbidite paleoseismology involves the use of marine or lacustrine turbidite recurrence rates as a
640 proxy for earthquake recurrence. This method has been applied to numerous settings to develop

641 estimates of long-term earthquake hazard rate (Adams, 1990; Monecke et al., 2004; Goldfinger et
642 al., 2007; Polonia et al., 2013; Moernaut et al., 2014, 2015). Sumner et al. (2013) outline four
643 independent criteria for identifying an earthquake trigger for turbidites: 1) synchronous turbidites in
644 multiple basins; 2) observing an identical number of turbidites above and below the confluence of
645 submarine channels; 3) identifying a larger relative volume for turbidites compared with others
646 deposited in the same setting; 4) a historical or observational record of an earthquake that is coeval
647 with the turbidite.

648

649 Nazaré canyon has three branching channels, with confluences at 500 and 3,000 m water depth (Fig.
650 2) (Lastras et al., 2009). There are no sediment cores positioned directly below or above these
651 confluences, making the confluence test of Adams (1990) unsuitable in this study area. Due to a lack
652 of core coverage in the basin it is also impossible to estimate turbidite volumes and invoke a seismic
653 trigger. Turbidite paleoseismology has been previously applied to the Iberian margin and a catalogue
654 of Late Quaternary seismo-turbidites exists for the Tagus and Horseshoe Basins (Fig. 10A) (Garcia-
655 Orellana et al., 2006; Gràcia et al., 2010; Masson et al., 2011b). This serves as a basis to test for
656 earthquake triggering of turbidites in the Iberian Abyssal Plain.

657

658 Comparison with published Iberian turbidite records reveals that only three turbidites correlate well
659 into the adjacent Tagus Abyssal Plain (TAP), and only one turbidite is well correlated in all three
660 basins (Fig. 10A). Other large turbidites from the Iberian Abyssal Plain (IAP) are not synchronous with
661 proposed seismo-turbidites from the Tagus or Horseshoe Abyssal Plain. The Iberian Margin contains
662 multiple faults as a result of the compressional rotation associated with the Azores-Gibraltar fracture
663 zone to the south (Fig. 10B) (Buforn et al., 1988; Borges et al., 2001; Zitellini et al., 2004; Custódio et
664 al., 2015). The Nazaré Fault (NF) and the Lower Tagus Valley Fault (LTVF) are quite proximal,
665 suggesting that large earthquakes originating from the LTVF might be capable of triggering sediment
666 failures which ignite and flush Nazaré Canyon (Fig. 10B) (Johnston, 1996). This could explain why
667 several turbidites are synchronous in both the Tagus and Iberian Abyssal Plains (Fig. 10A).

668

669 The tectonic regime along the south-western section of the Iberian Margin is more complicated, with
670 several extensive offshore faults capable of generating large earthquakes (Fig. 10B) (Pro et al., 2013;
671 Custódio et al., 2015). There is 300 km distance from the south-west margin to Nazaré Canyon, and
672 there is no continuous fault system between the areas. Paleoseismic intensity reconstructions and
673 seismic propagation models indicate large earthquakes along the south-western section of the
674 margin are unlikely to trigger canyon-flushing in Nazaré Canyon (Dobrovolsky et al., 1979; Buforn et
675 al., 1988; Fukushima and Tanaka, 1990; Johnston, 1996; Zitellini et al., 2004). This could explain why
676 several turbidites present in the Tagus and Horseshoe Abyssal Plain are not present in the Iberian
677 Abyssal Plain (Fig 10A).

678

679 The synchronous deposition test does not strongly support regional earthquakes as a trigger for
680 canyon-flushing turbidites in the Iberian Abyssal Plain. The historical record of large Portuguese
681 earthquakes extends back to the Portugal and Galicia Earthquake at 60 BC (Galbis, 1932; Baptista
682 and Miranda, 2009). Several earthquakes dating further back to 7,000 Cal years BP have been
683 inferred from onshore paleo-tsunami records (Ruiz et al., 2008). Importantly, these records place the
684 epicentres of many of these past earthquakes along the South-western Iberian Margin, and not
685 proximal to Nazaré Canyon. This also makes them unsuitable as an independent earthquake archive
686 with which to compare Iberian Abyssal Plain turbidite ages.

687

688 The Nazaré Fault (NF) forms part of a larger NNE-SSW-trending Variscan fault system which extends
689 across the peninsula (Fig. 10B) (Buforn et al., 1988; Zitellini et al., 2004). Paleoseismic
690 reconstructions on these NNE-SSW trending fault zones in Central and Northern Portugal are sparse,
691 and no such record exists for the Nazaré Fault. This makes identifying possible earthquake triggering
692 of canyon-flushing from nearby faults problematic. Optically Stimulated Luminescence (OSL) dates
693 from fault surfaces along the Manteigas-Bragança Fault (MBF) north-east of the Nazaré Fault reveal
694 three large (Mw 7.3) earthquakes between 11.5 and 14.5 \pm 2 ka, (Fig. 10A). These ages do not

695 correspond well with turbidites in the Iberian Abyssal Plain, although the wide margins of error do
696 encompass 2 turbidites at 11.7 ka and 14.9 ka (Fig. 10A). It has been proposed that these NNE-SSW-
697 trending Variscan faults primarily accommodate reverse faulting and not strike-slip faulting. In
698 contrast, WNW–ESE-trending faults on the South-western Iberian Margin exhibit strike-slip
699 behaviour (Borges et al., 2001; Custódio et al., 2015). This would imply that unlike the southwestern
700 margin, earthquakes along the Central Portuguese Margin do translate down-fault, limiting seismic
701 propagation (Sylvester, 1988).

702

703 A small number of turbidites from the Iberian Abyssal Plain can be correlated with seismo-turbidites
704 previously identified in the Tagus and Horseshoe Abyssal Plains (Fig. 10A). Turbidites which do not
705 correlate in the Tagus or Horseshoe Basins could be the result of earthquakes originating from
706 further north along the ENE-SSW Fault zone. However, given the wide uncertainties on earthquake
707 ages, and the structure of the fault system, any correlation with canyon-flushing events would be
708 largely speculative. There are multiple other intraplate faults that may trigger canyon-flushing, but
709 without accurate paleoseismic records it is impossible to imply causation (Buforn et al., 1988; Zitellini
710 et al., 2004; Villamor et al., 2012; Custódio et al., 2015). The lack of convincing evidence for
711 earthquake triggered canyon-flushing along this margin highlights the problems of applying turbidite
712 paleoseismology methods to structurally complex margins.

713

714 **5.3 Climate change and geohazard implications**

715

716 As previously outlined, many authors have suggested that large continental margin failures are
717 associated with times of significant climatic and sea level change (Maslin et al., 2004; Owen et al.,
718 2007; Lee, 2009; Smith et al., 2013; Brothers et al., 2013). One implication of this is that future
719 climate and sea level change might increase the frequency of large continental margin failures. Our
720 findings contribute to a growing body of literature that suggests large sediment failures in multiple
721 settings are temporally random and are not significantly influenced by climate or sea change (Beattie

722 and Dade, 1999; Urlaub et al., 2013, 2014; Clare et al., 2014; Hunt et al., 2014; Moernaut et al., 2014;
723 Talling et al., 2014). It might be reasonable to conclude that the recurrence intervals of large
724 sediment failures and canyon-flushing along the Central Iberian Margin will not be significantly
725 influenced by any future sea level rise. Canyon-flushing in other deep-sea canyons is currently poorly
726 understood and few estimates of recurrence rates exist. Additional work into other canyon systems
727 would help to determine if temporal randomness is a wide-spread characteristic of canyon-flushing.

728

729 Our statistical analysis demonstrates that sea level is a significant control on canyon-filling. However,
730 the current sea level highstand features limited canyon-filling events. These are typically small,
731 channel-confined turbidity currents that die before reaching the lower canyon (Fig 9A). Intuitively,
732 we might expect future sea level rise to further limit canyon-filling turbidity currents, as past sea
733 level rise did. However, future sea level rise has been predicted to increase rates of coastal erosion
734 (Gornitz, 1991; Bray and Hooke, 1997; Leatherman et al., 2000). This increase in sediment delivery to
735 the Iberian Shelf could lead to an increase in littoral transport into the head of Nazaré Canyon,
736 thereby promoting greater instability. These smaller turbidity currents may not have large geohazard
737 implications, but are important for assessing risk to seafloor structures such as pipelines and
738 telecommunication cables.

739

740 **6. Conclusions**

741

742 Canyon-flushing turbidity currents have been predicted to occur much less frequently than those
743 that fill canyons (Paull et al., 2005; Canals et al., 2006; Arzola et al., 2008; Puig, et al., 2014). Here we
744 demonstrate that canyon-flushing turbidity currents in this system have recurrence rates of several
745 thousands of years on average. This recurrence rate is an order of magnitude longer than those
746 filling the canyon during sea level lowstand, and more than two orders of magnitude longer than
747 those that fill the canyon in the present day. The recurrence intervals for canyon-filling and canyon-

748 flushing appear to have distinctly different statistical distributions. Moreover, unlike canyon filling,
749 the recurrence rate of canyon-flushing events does not appear to be affected by long-term changes
750 in sea level. This suggests that they may have different triggers, or that the signal of triggering
751 mechanisms is shredded due to the long recurrence intervals. From a geohazard assessment
752 perspective, this implies that the frequency of potentially hazardous canyon-flushing events may not
753 be influenced by future sea level predictions. The tectonic complexity of the margin, uncertainties in
754 age-control, and the time-independent behaviour of canyon-flushing make determining a trigger for
755 canyon-flushing problematic; although earthquakes may trigger some events.

756

757 Acknowledgements

758

759 The authors wish to thank Michele Rebesco, David Piper, and an anonymous reviewer. Their
760 comments and suggestions have greatly improved this manuscript. Financial support for this work
761 was provided by the Marine Geoscience group at the National Oceanography centre, and by the
762 NERC Arctic Research Programme (NE/K00008X/1). This research was completed as part of the EU
763 FP7-funded ASTARTE (Assessment, Strategy and Risk Reduction for Tsunamis in Europe) Project
764 (603839).

765

766 References:

767

768 Abraitmov, S.G., Turcotte, D.L., Shcherbakov, R., Rundle, J.B., Yakovlev, G., Goltz, C., Newman, W.I.,
769 2008. Earthquakes: Recurrence and interoccurrence times. *Pure and Applied Geophysics*
770 165, 777-795.

771 Adams, J., 1990. Paleoseismicity of the Cascadia subduction zone: Evidence from turbidites off the
772 Oregon-Washington margin. *Tectonics* 9, 569–583.

- 773 Ahmad, M.I., Sinclair, C.D., Werritty, A., 1988. Log-logistic flood frequency analysis. *Journal of*
774 *Hydrology* 98, 205-224.
- 775 Almeida, L.P., Ferreira, Ó., Vousdoukas, M.I., Dodet, G., 2011. Historical variation and trends in
776 storminess along the Portuguese South Coast. *Natural Hazards and Earth System Sciences*
777 11, 2407–2417.
- 778 Alves, T.M., Gawthorpe, R.L., Hunt, D.W., Monteiro, J.H., 2003. Cenozoic tectono-sedimentary
779 evolution of the western Iberian margin. *Marine Geology* 195, 75-108.
- 780 Arzola, R.G., Wynn, R.B., Lastras, G., Masson, D.G., Weaver, P.P.E., 2008. Sedimentary features and
781 processes in the Nazaré and Setúbal submarine canyons, west Iberian margin. *Marine*
782 *Geology* 250, 64-88.
- 783 Balsam, W.L., Deaton, B.C., Damuth, J.E, 1999. Evaluating optical lightness as a proxy for carbonate
784 content in marine sediment cores. *Marine Geology* 161, 141-153.
- 785 Baptista, M.A., Miranda, J.M., 2009. Revision of the Portuguese catalogue of tsunamis. *Natural*
786 *Hazards and Earth System Sciences* 9, 25–42.
- 787 Beattie, P. D., & Dade, W. B. (1996). Is scaling in turbidite deposition consistent with forcing by
788 earthquakes? *Journal of Sedimentary Research* 66 (5), 909-915.
- 789 Bondevik, S., Svendsen J.I., Johnsen, G, Mangerud, J and Kaland, P.E., 1997. The Storegga tsunami
790 along the Norwegian coast: Its age and run-up. *Boreas* 26, 29–53.
- 791 Borges, J., Fitas, A.J.S., Bezzeghoud, M. & Teves-Costa, P., 2001. Seismotectonics of Portugal and its
792 adjacent Atlantic area, *Tectonophysics* 331 (4), 373–387.
- 793 Bouma, A.H., 1962. *Sedimentology of some Flysch Deposits: A Graphic Approach to Facies*
794 *Interpretation*. Elsevier, Amsterdam, pp. 168.

- 795 Bray, M.J., Hooke, J.M., 1997. Prediction of soft-cliff retreat with accelerating sea-level rise. Journal
796 of Coastal Research 13 (2), 453-467.
- 797 Bronk Ramsey, C. *et al* et al., 2012. A Complete Terrestrial Radiocarbon Record for 11.2 to 52.8 kyr
798 B.P.. Science 338, 370-374.
- 799 Brushci, R., Bughi, S., Spinazzè, M., Torselletti, E., Vitali, L., 2006. Impact of debris flows and turbidity
800 currents on seafloor structures. Norwegian Journal of Geology 86, 317-337.
- 801 Buforn, E., Udías, A., Colombás, M.A., 1988. Seismicity, source mechanisms and tectonics of the
802 Azores-Gibraltar plate boundary. Tectonophysics 152, 89-118.
- 803 Canals, M., Puig, P., de Madron, X.D., Heussner, S., Palanques, A., Fabres, J., 2006. Flushing
804 submarine canyons. Nature 444, 354-357.
- 805 Carlson, A.E., Winsor, K., 2012. Northern hemisphere ice-sheet response to climate warming. Nature
806 Geoscience 5, 607-613.
- 807 Carter, L., Gavey, R., Talling, P.J., Liu, J., 2014. Insights into Submarine Geohazards from Breaks in
808 Subsea Telecommunication Cables. Oceanography 27 (2). 58-67.
- 809 Carter, L., Milliman, J.D., Talling, P.J., Gavey, R., Wynn, R.B., 2012. Near-synchronous and delayed
810 initiation of long run-out submarine sediment flows from a record-breaking river flood,
811 offshore Taiwan. Geophysical Research Letters 39 (12), doi:10.1029/2012GL051172.
- 812 Chappelle, J., 2002. Sea level changes forced ice breakouts in the Last Glacial cycle: new results from
813 coral terraces. Quaternary Science Reviews 21, 1229-1240.
- 814 Clare, M. A., Talling, P. J., Challenor, P. G., & Hunt, J. E. (2016). Tempo and Triggering of Large
815 Submarine Landslides: Statistical Analysis for Hazard Assessment. In Submarine Mass
816 Movements and their Consequences. Springer International Publishing, pp. 509-517.

- 817 Clare, M A., Talling, P.J., Hunt, J.E., 2015. Are landslide-turbidite recurrence intervals random and
818 what are the implications of a common distribution for triggers, regional controls and
819 climate influence? *Earth and Planetary Science Letters* 420, 102-115.
- 820 Clare, M.A., Talling, P.J., Challenor, P., Malgesini, G., Hunt, J.E., 2014. Distal turbidites reveal a
821 common distribution for large (>0.1 km³) submarine landslide recurrence. *Geology* 42 (3),
822 263-266.
- 823 Clark, P.U., Dyke, A.S., Shakun, J.D., Carlson, A.E., Clark, J., Wohlfarth, B., Mitrovica, J.X., Hostetler,
824 S.W., McCabe, A.M., 2009. The Last Glacial Maximum. *Science* 325, 710-714.
- 825 Clark, P.U., McCabe, A.M., Mix, A.C., Weaver, A.J., 2004. Rapid rise of sea level 19,000 years ago and
826 its global implications. *Science* 304, 1141-1144.
- 827 Clark, P.U., Mix, A.C., 2000. Ice sheets by volume. *Nature* 406, 689–690.
- 828 Covault, J.A., & Fildani, A., 2014. Continental shelves as sediment capacitors or conveyors: source-to-
829 sink insights from the tectonically active Oceanside shelf, southern California, USA.
830 *Geological Society of London Memoirs* 41.1, 315–326.
- 831 Covault, J.A., Graham, S.A., 2010. Submarine fans at all sea-level stands: Tectono-morphologic and
832 climatic controls on terrigenous sediment delivery to the deep sea. *Geology* 38, 939-942.
- 833 Covault, J.A., Romans, B.W., Fildani, A., McGann, M., & Graham, S.A., 2010. Rapid climatic signal
834 propagation from source to sink in a southern California sediment-routing system. *Journal of*
835 *the Geological Society of America* 118, 247–259.
- 836 Cox, D.R., 1972. Regression models and life-tables. *Journal of the Royal Statistical Society, Series B*,
837 187-220.

- 838 Croudace, I.W., Rindby, A., Rothwell, G., 2006. ITRAX: description and evaluation of a multi-function
839 X-ray core scanner. In: Rothwell, R.G. (Ed.), *New techniques in sediment core analysis*.
840 Geological Society of London Special Publications 267, pp. 51–63.
- 841 Custódio, S., Dias, N.A., Carrilho, F., Góngora, E., Rio, I., Marreiros, C., Morais, I., Alves, P., Matias, L.,
842 2015. Earthquakes in western Iberia: improving the understanding of lithospheric
843 deformation in a slowly deforming region. *Geophysical Journal International* 203, 127-145.
- 844 de Stigter, H.C., Boer, W., de Jesus Mendes, P.A., César Jesus, C., Thomsen, L., van der Bergh, G.D.,
845 van Weering, T.C.E., 2007. Recent sediment transport and deposition in the Nazaré Canyon,
846 Portuguese continental margin. *Marine Geology* 246, 144-164.
- 847 de Stigter, H.C., Jesus, C.C., Boer, W., Richter, O.T., Costa, A., van Weering, T.C.E., 2011. Recent
848 sediment transport and deposition in the Lisbon-Setúbal and Cascais submarine canyons,
849 Portuguese continental margin. *Deep Sea Research II* 58 (23), 2321–2344.
- 850 Dobrovolsky, I.P., Zubkov, S.I., Miachkin, V.I., 1979. Estimation of the size of earthquake preparation
851 zones. *Pure and Applied Geophysics* 117 (5), 1025-1044.
- 852 Ducassou, E., Migeon, S., Mulder, T., Murat, A., Capotondi, L., Bernasconi, S.M., Mascle, J., 2009.
853 Evolution of the Nile deep-sea turbidite system during the Late Quaternary: influence of
854 climate change on fan sedimentation. *Sedimentology* 56, 2061-2090.
- 855 Durán, R., Canals, M., Lastras, G., Micallef, A., Amblas, D., Pedrosa-Pàmies, R., Sanz, J.S., 2013.
856 Sediment dynamics and post-glacial evolution of the continental shelf around the Blanes
857 submarine canyon head (NW Mediterranean). *Progress in Oceanography* 118, 28-46.
- 858 Fukushima, Y., Tanaka, T., 1990. A new attenuation relation for peak horizontal acceleration of
859 strong earthquake ground motion in Japan. *Bulletin of the Seismological Society of America*
860 80 (4), 757-778.

- 861 Galbis, J., 1932. Cata'logo sísmico de la zona comprendida entre los meridianos 5° E y 20° W de
862 Greenwich y los paralelos 45° y 25° N, Tomo 1. Instituto Geográfico, Catastral y de
863 Estadística, Madrid. 897pp.
- 864 Garcia-Orellana, J., et al., 2006. Identifying instrumental and historical earthquake records in the SW
865 Iberian Margin using 210Pb turbidite chronology. *Geophysical Research Letters* 33, L24601.
866 <http://dx.doi.org/10.1029/2006GL028417>.
- 867 Goldfinger, C., Morey, A.E., Nelson, C.H., Gutiérrez-Pastor, J., Johnson, J.E., Karabanov, E., Chaytor, J.,
868 Eriksson, A., 2007. Rupture lengths and temporal history of significant earthquakes on the
869 offshore and north coast segments of the Northern San Andreas Fault based on turbidite
870 stratigraphy. *Earth and Planetary Science Letters* 254, 9–27.
- 871 Gornitz, V., 1991. Global coastal hazards from future sea level rise. *Palaeogeography,*
872 *Palaeoclimatology, Palaeoecology (Global Planetary Change Section)* 89, 379-398.
- 873 Gràcia, E., Vizciano, A., Escutia, C., Asioli, A., Rodés, Á., Pallàs, R., Garcia-Orellana, J., Lebreiro, S.,
874 Goldfinger, C., 2010. Holocene earthquake record offshore Portugal (SW Iberia): testing
875 turbidite paleoseismology in a slow-convergence margin. *Quaternary Science Reviews* 29,
876 1156-1172.
- 877 Green, S.B., 1991. How many subjects does it take to do a regression analysis? *Multivariate*
878 *Behavioral Analysis* 26 (3), 499-510.
- 879 Gutiérrez-Pastor, J., Nelson, C.H., Goldfinger, C., Johnson, J.E., Escutia, C., Eriksson, A., Morey, A.E.,
880 and the Shipboard Scientific Party, 2009. Earthquake control of Holocene turbidite frequency
881 confirmed by hemipelagic sedimentation chronology on the Cascadia and Northern
882 California active tectonic continental margins. In: Kneller, B., McCaffrey, W., Martinsen, O.J.
883 (Eds.), *External Controls on Deepwater Depositional Systems*. SEPM Special Publication, v.
884 92. Society for Sedimentary Geology, Tulsa, OK, ISBN 978-1-56576-136-0, p. 179–197.

- 885 Hagiwara, Y., 1974. Probability of earthquake occurrence as obtained from a Weibull distribution
886 analysis of crustal strain. *Tectonophysics* 23, 313-318.
- 887 Hoogakker, B.A.A., Rothwell, R.G., Rohling, E.J., Paterne, M., Stow, D.A.V., Herrle, J.O., Clayton, J.,
888 2004. Variations in terrigenous dilution in western Mediterranean Sea pelagic sediments in
889 response to climate change during the last glacial cycle. *Marine Geology* 211, 21-43.
- 890 Hunt, J.E., Talling, P.J., Clare, M.A., Jarvis, I., Wynn, R.B., 2014. Long-term (17 Ma) turbidite record of
891 the timing and frequency of large flank collapses of the Canary Islands. *Geochemistry,*
892 *Geophysics, Geosystems* 15 (8), 3322-3345.
- 893 Hunt, J.E., Wynn, R.B., Talling, P.J., Masson, D.G., 2013a. Frequency and timing of landslide-triggered
894 turbidity currents within the Agadir Basin, offshore NW Africa: Are there associations with
895 climate change, sea level change and slope sedimentation rates? *Marine Geology* 346, 274-
896 291.
- 897 Hunt, J.E., Wynn, R.B., Talling, P.J., Masson, D.G., 2013b. Multistage collapse of eight western Canary
898 Island landslides in the last 1.5 Ma: Sedimentological and geochemical evidence from
899 subunits in submarine flow deposits. *Geochemistry, Geophysics, Geosystems* 14, 2159–2181.
- 900 Ingersoll, R. V., Dickinson, W. R., & Graham, S. A., 2003. Remnant-ocean submarine fans: largest
901 sedimentary systems on Earth. *Special Papers - Geological Society of America*, 191-208.
- 902 IOC, IHO, BODC,. 2003. Centenary Edition of the GEBCO Digital Atlas. British Oceanographic Data
903 Centre, Liverpool.
- 904 Jerolmack, D.J., Paola, C., 2010. Shredding of environmental signals by sediment transport.
905 *Geophysical Research Letters* 37, L19401, doi:10.1029/2010GL044638,
- 906 Johnston, A.C., 1996. Seismic moment assessment of earthquakes in stable continental regions-111.
907 New Madrid 181 1-1812, Charleston 1886 and Lisbon 1755. *Geophysical Journal*
908 *International* 126, 314-344.

- 909 Jorry, S.J., Jégou, I., Emmanuel, L., Silva Jacinto, R., Savoye, B., 2011. Turbiditic levee deposition in
910 response to climate changes: The Var Sedimentary Ridge (Ligurian Sea), *Marine Geology* 279,
911 148-161.
- 912 Khripounoff, A., Vangriesheim, A., Crassous, P., Etoubleau, J., 2009. High frequency of sediment
913 gravity flow events in the Var submarine canyon (Mediterranean Sea). *Marine Geology* 263,
914 1–6.
- 915 Lambeck, K., Rouby, H., Purcell., P., Sun, Y., Sambridge, S., 2014. Sea level and global ice volumes
916 from the Last Glacial Maximum to the Holocene. *Proceedings of the National Academy of*
917 *Sciences* 111 (43), 15296-15303.
- 918 Lastras, G., Arzola, R.G., Masson, D.G., Wynn, R.B., Huvenne, V.A.I., Hühnerbach, V., Canals, M.,
919 2009. Geomorphology and sedimentary features in the Central Portuguese submarine
920 canyons, Western Iberian margin. *Geomorphology* 103, 310-329.
- 921 Leatherman, S.P., Zhang, K., Douglas, B.C., 2000. Sea level rise shown to drive coastal erosion. *Eos*
922 *Transactions of the American Geophysical Union* 81, 55-57.
- 923 Lebreiro, S.M., McCave, I.N., Weaver, P.P.E., 1997. Late Quaternary turbidite emplacement on the
924 Horseshoe abyssal plain (Iberian margin). *Journal of Sedimentary Research* 67, 856–870.
- 925 Lebreiro, S.M., Voelker, A.H.L., Vizcaino, A., Abrantes, F.G., Alt-Epping, U., Jung, S., Thouveny, N.,
926 Grácia, E., 2009. Sediment instability on the Portuguese continental margin under abrupt
927 glacial climate changes (last 60 kyr). *Quaternary Science Reviews*. 28, 3211–3223.
- 928 Lee, H.J., 2009. Timing of occurrence of large submarine landslides on the Atlantic ocean margin,
929 *Marine Geology* 264, 56-64.
- 930 Lehmann, E.L., D'Abrera, H., 2006. *Nonparametrics: Statistical methods based on ranks*, Springer,
931 New York.

- 932 Lozano, I., Devoy, R.J.N., May, W., Anderson, U., 2004. Storminess and vulnerability along the
933 Atlantic coastlines of Europe: analysis of storm records and of a greenhouse gases induced
934 climate scenario. *Marine Geology* 210, 205-225.
- 935 Marshall, N.F., 1978. Large storm-induced sediment slump reopens an unknown Scripps submarine
936 canyon tributary. In: Stanley, D.J., Kelling, G. (Eds.), *Sedimentation in Submarine Canyons,*
937 *Fans and Trenches.* Dowden, Hutchinson and Ross Inc., Pennsylvania, pp. 73–82.
- 938 Martin, J., Palanques, A., Vitorino, J., Oliveira, A., de Stitger, H.C., 2011. Near-bottom particulate
939 matter dynamics in the Nazaré submarine canyon under calm and stormy conditions. *Deep-*
940 *Sea research II* 58, 2388-2400.
- 941 Maslin, M., Owen, M., Day, S., Lond, D., 2004. Linking continental slope-failures and climate change:
942 testing the clathrate gun hypothesis. *Geology* 32 (1), 53-56.
- 943 Masson, D.G., Arzola, R.G., Wynn, R.B., Hunt, J.E., Weaver, P.P.E., 2011b. Seismic triggering of
944 landslides and turbidity currents offshore Portugal. *Geochemistry, Geophysics, Geosystems*
945 12, doi:10.1029/2011GC003839.
- 946 Masson, D.G., Harbitz, C.B., Wynn, R. B., Pedersen, G. and Løvholt, F., 2006. Submarine landslides:
947 processes, triggers and hazard prediction. *Philosophical Transactions of the Royal Society*
948 364, 2009–2039.
- 949 Masson, D.G., Huvenne, V.A.I., de Stigter, H.C., Arzola, R.G., LeBas, T.P., 2011a. Sedimentary features
950 in the middle Nazaré Canyon. *Deep-Sea Research II* 58, 2369-2387.
- 951 McCullagh, P., Nelder, J.A., 1989. *Generalized Linear Models, Second Edition.* Chapman and Hall/CRC,
952 London.
- 953 Mecklin, C., 2007. Q-Q Plot. In: Salkind, N.J., Rasmussen, K. (Eds.), *Encyclopedia of Measurement and*
954 *Statistics.* Thousand Oaks, CA: Sage Publications, Inc., pp. 803-805. doi:
955 <http://dx.doi.org/10.4135/9781412952644.n367>

- 956 Milkert, D., Alonso, B., Liu, L., Zhao, X., Comas, M., de Kaenel, E., 1996a. Sedimentary facies and
957 depositional history of the Iberia Abyssal Plain. In: Whitmarsh, R.B., Sawyer, D.S., Klaus, A.,
958 and Masson, D.G.. Proceedings of the Ocean Drilling Program, Scientific Results 149, Ch. 45,
959 685-704.
- 960 Milkert, D., Weaver, P.P.E., Liu, L., 1996b. Pleistocene and Pliocene turbidites from the Iberia Abyssal
961 Plain. In: Whitmarsh, R.B., Sawyer, D.S., Klaus, A., and Masson, D.G., Proceedings of the
962 Ocean Drilling Program, Scientific Results, 149, Ch. 12, 281-294.
- 963 Moernaut, J., Van Daele, M., Strasser, M., Clare, M.A., Heirman, K., Viel, M., Cardenas, J., Kilian, R.,
964 Ladrón de Guevara, B., Pino, M., Urrutia, R., De Batist, M. (2015) Lacustrine turbidites
965 produced by surficial slope sediment remobilization: a mechanism for continuous and
966 sensitive turbidite paleoseismic records. *Marine Geology*. [doi:10.1016/j.margeo.2015.10.009](https://doi.org/10.1016/j.margeo.2015.10.009)
- 967 Moernaut, et al (2014). Lacustrine turbidites as a tool for quantitative earthquake reconstruction:
968 New evidence for a variable rupture mode in south central Chile. *Journal of Geophysical*
969 *Research: Solid Earth*, 119 (3), 1607-1633.
- 970 Monecke, K., Anselmetti, F.S., Becker, A., Sturm, M., Giardini, D., 2004. Signature of historic
971 earthquakes in lake sediments in Central Switzerland. *Tectonophysics* 394, 21–40.
- 972 Monges Soares, A.M., 1993. The ^{14}C content of marine shells: Evidence for variability in coastal
973 upwelling off Portugal during the Holocene in Isotope techniques. In: *The Study of Past and*
974 *Current Environmental Changes in the Hydrosphere and Atmosphere (Proceedings) Vienna*.
975 IAEA-SM-329/49. 471-485.
- 976 Naylor, M.A., 1980. Origin of inverse grading in muddy debris flow deposits--a review. *Journal of*
977 *Sedimentary Petrology* 50, 1111-6.

- 978 Normark, W.R., Piper, D.J.W., 1991. Initiation processes and flow evolution of turbidity currents:
979 implications for the depositional record. In: From Shoreline to Abyss, edited by R.H. Osborne,
980 Special Publications SEPM Society for Sedimentary Geology 46, 207 – 230.
- 981 Oliveira, A., Santos, A.I., Rodrigues, A., Vitorino, J., 2007. Sedimentary particle distribution and
982 dynamics on the Nazaré canyon system and adjacent shelf (Portugal). *Marine Geology* 246,
983 105-122.
- 984 Owen, M., Day, S., Maslin, M., 2007. Late Pleistocene submarine mass movements: occurrence and
985 causes. *Quaternary Science Reviews* 26, 958–978.
- 986 Parker, G., 1982. Conditions for the ignition of catastrophically erosive turbidity currents. *Marine*
987 *Geology* 46, 307-327.
- 988 Parzen, E., 1962. On estimation of a probability density function and mode. *Annals of Mathematics*
989 *and Statistics* 33 (3), 1065–1076.
- 990 Peltier, W., Fairbanks, R., 2006. Global glacial ice volume and Last Glacial Maximum duration from an
991 extended Barbados sea level record. *Quaternary Science Reviews* 25, 3322–3337.
- 992 Pinder III, J.E., Wiener, J.G., Smith, M.H., 1978. The Weibull distribution: a new method of
993 summarizing survivorship data. *Ecology* 59 (1), 175-179.
- 994 Piper, D.J.W., Savoye, B., 1993. Processes of late Quaternary .turbidity current flow and deposition
995 on the Var deep-sea fan, north-west Mediterranean Sea. *Sedimentology* 40, 557-582.
- 996 Piper, D.W.J, Bowen, A.J., 1978. Origin of lamination in deep sea, fine-grained sediments. *Nature*
997 274, 324-328.
- 998 Piper, D.W.J., Normark, W.R., 2001. Sandy fans—from Amazon to Hueneme and beyond: AAPG
999 Bulletin 85 (8), 1407-1438.

- 1000 Piper, D.W.J., Normark, W.R., 2009. Processes that initiate turbidity currents and their influence on
1001 turbidites: a marine geology perspective. *Journal of Sedimentary Research* 79, 347-362.
- 1002 Polonia, A., Panieri, G., Gasperini, L., Gasparotto, G., Bellucci, L.G., Torelli, L., 2013a. Turbidite
1003 paleoseismology in the Calabrian Arc subduction complex (Ionian Sea). *Geochemistry,
1004 Geophysics, Geosystems* 14, 112–140.
- 1005 Pope, E.L., Talling, P.J., Urlaub, M., Hunt, J.E., Clare, M.A., Challenor, P., 2015. Are large submarine
1006 landslides temporally random or do uncertainties in available age constraints make it
1007 impossible to tell? *Marine Geology* 369, 19-33.
- 1008 Posamentier, H.W., Erskine, R.D., and Mitchum, R.M., Jr., 1991. Submarine fan deposition within a
1009 sequence stratigraphic framework. In: Weimer, P., and Link, M.H., eds., *Seismic facies and
1010 sedimentary processes of submarine fans and turbidite systems*. New York, Springer-Verlag,
1011 p. 127–136.
- 1012 Pro, C., Buforn, E., Bezzeghoud, M., Udias, A., 2013. Mechanism of 2003, 2007 and 2009 earthquakes
1013 (S. Vicente Cape) and implications for the 1755 Lisbon earthquake. *Tectonophysics* 583, 16–
1014 27.
- 1015 Puig, P., Palanques, A., Martin, J., 2014. Contemporary sediment-transport processes in submarine
1016 canyons. *Annual Review of Marine Science* 6, 5.1-5.25.
- 1017 Ratzov, G., Cattaneo, A., Babonneau, N., Déverchère, J., Yelles, K., Bracene, R., & Courboulex, F.
1018 (2015). Holocene turbidites record earthquake supercycles at a slow-rate plate boundary.
1019 *Geology* 43 (4), 331-334.
- 1020 Reimer, P.J., Bard, E., Bayliss, A., Beck, J.W., Blackwell, P.G., Ramsey, C.B., Buck, C.E., Cheng, H.,
1021 Edwards, R.L., Friedrich, M., Grootes, P.M., Guilderson, T.P., Hafliðson, H., Hajdas, I., Hatté,
1022 C., Heaton, T., Hoffmann, D.L., Hogg, A., Hughen, K.A., Kaiser, K., Kromer, B., Manning, S.W.,
1023 Niu, M., Reimer, R., Richards, D.A., Scott, E.M., Southon, J.R., Staff, R.A., Turney, C., Plicht, J.,

- 1024 2013. IntCal13 AND Marine13 radiocarbon age calibration curves 0–50,000 years cal BP.
1025 Radiocarbon 55, 1869-1887.
- 1026 Rockwell, T., Fonseca, J., Madden, C., Dawson, T., Owen, L.A., Vilanova, S. & Figueiredo, P., 2009.
1027 Palaeoseismology of the Vilariça Segment of the Manteigas-Bragança Fault in northeastern
1028 Portugal, Geological Society, London, Special Publications 316 (1), 237–258.
- 1029 Romans, B.W., Castelltort, S., Covault, J.A., Fildani, A., Walsh, J.P., 2015. Environmental signal
1030 propagation in sedimentary systems across timescales. Earth-Science Reviews
1031 doi:10.1016/j.earscirev.2015.07.012.
- 1032 Ruiz, F., Abad, M., Vidal, J.R., Ca´ceres, L.M., González-Regalado, M.L., Carretero, M.I., Pozo, M.,
1033 Toscano, F.G., 2008. The geological record of the oldest historical tsunamis in southwestern
1034 Spain. *Rivista Italiana di Paleontologia e Stratigrafia* 114 (1), 145–154.
- 1035 Shanmugam, G., Moiola, R.J., 1982. Eustatic control of turbidites and winnowed turbidites. *Geology*
1036 10, 231–235.
- 1037 Shanmugam, G., Bloch, R.B., Mitchell, S.M., Beamish, G.W.J., Hodgkinson, R.J., Damuth, J.E.,
1038 Straume, T., Syvertsen, S.E., Shields, K.E., 1995. Basin-Floor Fans in the North Sea: Sequence
1039 Stratigraphic Models vs. Sedimentary Facies. *AAPG Bulletin* 79 (4), 477-512.
- 1040 Smith, D.E., Harrison, S., Jordan, D.T., 2013. Sea level rise and submarine mass failure on open
1041 continental slopes. *Quaternary Science Reviews* 82, 93-103.
- 1042 Sommerfield, C.K., Lee, H.J., 2004. Across-shelf sediment transport since the Last Glacial Maximum,
1043 southern California margin. *Geology* 32, 345-348.
- 1044 Stephens, M.A., 1974. EDF statistics for goodness of fit and some comparisons. *Journal of the*
1045 *American Statistical Association* 69 (347), 730-737.

- 1046 Stow, D.A.V., and Piper, D.J.W., 1984. Deep-water fine-grained sediments: facies models. In Stow,
1047 D.A.V., and Piper, D.J.W. (Eds.). *Fine-grained sediments: deep-water processes and facies*.
1048 Special Publications, Geological Society of London, 14, pp. 611-645.
- 1049 Stow, D.A.V., Howell, D.G., and Nelson, C.H., 1985. Sedimentary, tectonic, and sea-level controls, in
1050 Bouma, A.H., et al., eds., *Submarine fans and related turbidite systems*. New York, Springer,
1051 p. 15–22.
- 1052 Stow, D.A.V., Howell, D.G., Nelson, C.H., 1984. Sedimentary, Tectonic, and Sea-Level Controls on
1053 Submarine Fan and Slope-Apron Turbidite Systems. *Geo-Marine Letters* 3, 57-64.
- 1054 Stow, D.A.V., Shanmugam, G., 1980. Sequence of structures in fine-grained turbidites: comparison of
1055 recent deep-sea and ancient flysch sediments. *Sedimentary Geology* 25, 23–42.
- 1056 Sumner, E.J., Siti, M.I., McNeill, L.C., Talling, P.J., Henstock, T.J., Wynn, R.B., Djajadihardja, Y.S.,
1057 Permana, H., 2013. Can turbidites be used to reconstruct a paleoearthquake record for the
1058 central Sumatran margin? *Geology*, doi:10.1130/G34298.1
- 1059 Swan, A.R.H., Sandilands, M., 1995. *Introduction to Geological Data Analysis*. Blackwell Science,
1060 Oxford; Cambridge, Mass, USA.
- 1061 Sylvester, A.G., 1988. Strike-slip faults. *Geological Society of America Bulletin* 100, 1666-1703.
- 1062 Tabachnick, B.G. and Fidell, L.S., 2007. *Using Multivariate Statistics*, Fifth Edition, Boston: Pearson
1063 Education, Inc.
- 1064 Talling, P.J., 2014. On the triggers, resulting flow types and frequencies of subaqueous sediment
1065 density flows in different settings. *Marine Geology* 352, 155-182
- 1066 Talling, P., Clare, M., Urlaub, M., Pope, E., Hunt, J., & Watt, S. (2014). Large Submarine Landslides on
1067 Continental Slopes: Geohazards, Methane Release, and Climate Change. *Oceanography*, 27
1068 (2), 32-45.

- 1069 Talling, P.J., Masson, D.G., Sumner, E.J., Malgesini, G., 2012. Subaqueous sediment density flows:
1070 depositional processes and deposit types. *Sedimentology* 59, 1937-2003.
- 1071 Talling, P.J., Paull, C.K., Piper, D.J.W. 2013. How are subaqueous sediment density flows triggered,
1072 what is their internal structure and how does it evolve? Direct observations from monitoring
1073 of active flows. *Earth-Science Reviews* 125. 244-287.
- 1074 Thomson, J., and Weaver, P.P.E., 1994. An AMS Radiocarbon method to determine the emplacement
1075 time of recent deep-sea turbidites. *Sedimentary Geology* 89, 1–7.
- 1076 Tsutsui, B., Campbell, J.F., Coulbourn, W.T., 1987. Storm-generated, episodic sediment movements
1077 off Kahe Point, Oahu, Hawaii. *Marine Geology* 76, 281–299.
- 1078 Urlaub, M., Talling, P., & Clare, M. (2014). Sea-level-induced seismicity and submarine landslide
1079 occurrence: Comment. *Geology* 42 (6), 337.
- 1080 Urlaub, M., Talling, P. J., & Masson, D. G. (2013). Timing and frequency of large submarine landslides:
1081 implications for understanding triggers and future geohazard. *Quaternary Science Reviews*
1082 72, 63-82.
- 1083 Vail, P.R., Mitchum, R.M.J., Todd, R.G., Widmier, J.M., Thompson, S.I., Sangree, J.B., Bubb, J.N.,
1084 Hatelid, W.G., 1977. Seismic stratigraphy and global changes of sea level. In: Payton, C.E.
1085 (Ed.), *Seismic Stratigraphy – Applications to Hydrocarbon Exploration*. AAPG Mem., vol. 26.
1086 American Association of Petroleum Geologists, Tulsa, Ok, pp. 49–212.
- 1087 van Rooij, M.M., Nash, B.A., Rajaraman, S., Holden, J.G., 2013. A fractal approach to dynamic
1088 inference and distribution analysis. *Frontiers in Physiology* 4.
- 1089 van Weering, T.C.E., de Stigter, H.C., Boer, W., de Haas, H., 2002. Recent sediment transport and
1090 accumulation on the NW Iberian margin. *Progress in Oceanography* 52, 349-371

- 1091 Vanney, J-R., Mougnot, D., 1990. Un canyon sous-marin du type 'gouf': le Canhao da Nazare'
1092 (Portugal). *Oceanologica Acta* 13, 1–14
- 1093 Villamor, P., Capote, R., Stirling, M.W., Tsige, T., Berryman, K.R., Martinez-Diaz, J.J., Martin-González,
1094 F., 2012. Contribution of active faults in the intraplate area of Iberia to seismic hazard: The
1095 Alentejo-Plasencia Fault. *Journal of Iberian Geology* 38 (1), 85-111.
- 1096 Vittinghoff, E., and C. E. McCulloch (2007), Relaxing the rule of ten events per variable in logistic and
1097 Cox regression, *American Journal of Epidemiology*, 165(6), 710.
- 1098 Weaver, P. P. E., 1994. Determination of turbidity current erosional characteristics from reworked
1099 coccolith assemblages, Canary Basin, north-east Atlantic. *Sedimentology* 41, 1025–1038.
- 1100 Weaver, P.P.E., Thomson, J., 1993. Calculating erosion by deep-sea turbidity currents during
1101 initiation and flow. *Nature* 364, 136–138.
- 1102 Wynn, R.B., Weaver, P.P.E., Stow, D.A.V., Masson, D.G., 2002. Turbidite depositional architecture
1103 across three interconnected deep-water basins on the northwest African margin.
1104 *Sedimentology* 49, 1441–1462.
- 1105 Xu, J.P., Noble, M.A., Rosenfeld, L.K., 2004. In-situ measurements of velocity structure within
1106 turbidity currents. *Geophysical Research Letters* 31, L09311, doi:10.1029/2004GL019718.
- 1107 Zitellini, N., Rovere, M., Terrinha, P., Chierici, F., Matias, L., and Bigsets Team, 2004. Neogene
1108 Through Quaternary Tectonic Reactivation of SW Iberian Passive Margin. *Pure and Applied*
1109 *Geophysics* 161, 565–587.
- 1110
- 1111 Figures and Tables:
- 1112
- 1113 Fig. 1: Map of the Portuguese Margin, showing the location of the main sedimentary basins and their
1114 feeder canyons. Core JC27-51, located in the distal Iberian Abyssal Plain is also shown. Bathymetry
1115 data are from the GEBCO database (IOC, IHO, BODC, 2003).

1116

1117 Fig. 2: Location map of the Nazaré Canyon and the locations of canyon cores used in this study.

1118

1119 Fig. 3: Lithological description of the cores used in this study. Dark grey represents turbidite mud,
1120 orange represent silt and yellow represents sand. Radiocarbon dates and their core positions are
1121 indicated with black arrows.

1122

1123 Fig. 4: Bed types present in JC27 sediment cores. JC27-51: (A) Thick mud-dominated turbidites with
1124 bioturbated mud caps, (B) thick sand rich turbidites with discernible Bouma (T) divisions, and (C) a
1125 debrite with mud and silt clasts. JC27-46: (D) The upper 6 m of the core is composed of thin sand or
1126 silt-based turbidite with a dominant mud unit and hemipelagic sediment intervals. (E) The lower 6m
1127 is mainly composed of thin-bedded sand rich turbidites with a thinner mud cap and sparse
1128 hemipelagic sediment. JC27-47: Turbidites are typically (F) planar and often erosive, or (G) chaotically
1129 structured, with reverse grading, overturned layers and evidence of scouring.

1130

1131 Fig. 5: Hemipelagic material and turbidites present within cores JC27-51 and JC27-46. ITRAX Calcium
1132 records assist in defining the boundaries between pure hemipelagite and bioturbated turbidite mud
1133 cap in JC27-51. There are no ITRAX data for JC27-46, but hemipelagite can still be defined by the
1134 presence of a colour change and dark mottling.

1135

1136 Fig. 6: hemipelagic aGe models for cores JC27-51 and JC27-46. R^2 values indicate minimal deviation
1137 from the line and thus a relatively stable hemipelagic sedimentation rate in both cores. This serves as
1138 a reasonable basis for using a stable sedimentation rate to interpolate between radiocarbon dates
1139 and further back in the record beyond radiocarbon age.

1140

1141 Fig. 7. **A:** Frequency of turbidites contained within core external levee JC27-46. Turbidites are binned
1142 into 500 year intervals and plotted against global eustatic sea level curves. Trend suggests near

1143 shutdown of large canyon-filling turbidites recorded in the levee following the onset of sea level
1144 highstand at 7 ka. **B**: Frequency of turbidites from internal levee core JC27-47. It illustrates a similar
1145 pattern of decline through sea level transgression and into the present-day highstand. H1-3 =
1146 Heinrich events. YD = Younger Dryas.

1147

1148 Fig. 8: Comparison of Iberian Abyssal Plain recurrence intervals with published recurrence intervals
1149 from several long-term basin records in Clare et al. (2014). The vertical axis plots the probability (P)
1150 that a given turbidite recurrence interval value (time since last event, T) will exceed the average
1151 recurrence interval for its respective dataset. The horizontal axis plots normalised recurrence interval
1152 data. The recurrence intervals are normalized by subdividing each recurrence interval (T) by the
1153 mean recurrence interval (λ) for each of the data sets to plot a dimensionless variable, R_T . N =
1154 number of events in each basin data series.

1155

1156 Fig. 9: Schematic displaying the spatial and temporal variability in turbidity current frequency in
1157 Nazaré Canyon during periods of sea level lowstand and highstand. **A**: During the present day
1158 highstand canyon-filling turbidity currents (TCs) are frequent in the upper canyon, but only small
1159 thalweg-confined turbidity currents reach to greater than 4,000 m water depth. **B**: During lowstand
1160 conditions canyon-filling turbidity currents were much larger, were able to reach the lower canyon,
1161 and regularly over-spilled canyon levees. Infrequent canyon-flushing turbidity currents were not
1162 affected by changes in sea level and continued into the present-day highstand.

1163

1164 Fig. 10. **A**: Proposed seismoturbidites from the Tagus and Horseshoe Abyssal Plains from Grácia et al.
1165 (2010) and Masson et al. (2011b) (shown as black dots). Turbidites from the Iberian Abyssal Plain are
1166 shown in red, and paleoearthquakes from the Manteigas-Braçanga Fault are shown in blue. Orange
1167 bars represent event which can be correlated based on their age uncertainties. Dashed error bars on
1168 ages represent ages that are determined through linear interpolation. **B**: Map of the Portuguese
1169 Margin showing primary structural faults. MTB = Manteigas-Braçanga Fault, NF = Nazaré Fault, LTVF

1170 = Lower Tagus Valley Fault, MF = Messejana Fault, PSF = Pereira de Sousa Fault, MPTF - Marquês de
1171 Pombal Thrust Fault, HTF = Horseshoe Thrust Fault, GTF = Gorringe Thrust Fault, SWIM = South-
1172 western Iberian Margin lineaments. Labels in italics indicate locations of paleoseismic
1173 reconstructions in Fig. 10A.

1174

1175 Table 1: List of radiocarbon samples used in this study. Note: Cal BP ages from D15738 and D15739
1176 (Masson et al, 2011a) are median values, and not determined using maximum probability.

1177

1178 Table 2: Core JC27-51 turbidites, their projected ages, and recurrence interval determined using a
1179 linear age model.

1180

1181 Supplementary table 1: Hemipelagic thicknesses, hemipelagic linear age model and interpolated ages
1182 for turbidites in levee core JC27-46.

1183

1184 Supplementary table 2: Model outputs from both the generalised linear models and Cox
1185 proportional hazards models testing the influence of sea level on turbidite recurrence and frequency
1186 in levee core JC27-46. Asterisks represent the significance of the p-values, with '****' being the
1187 highest significance, and no asterisks indicating no significance of sea level as an explanatory
1188 variable. Q-Q plot fits are indicated as Very poor, Poor, Moderate, or Good. The results indicate that
1189 sea level is a significant explanatory variable for changes in turbidite recurrence and frequency.

1190

1191 Supplementary table 3 Model output for Mann-Whitney and Kolgomorov-Smirnoff tests of the
1192 distribution of Iberian Abyssal Plain turbidite recurrence in core JC27-51 vs. those of other basin
1193 plains and levee core JC27-46. The results indicate that the distribution of recurrence intervals in the
1194 Iberian Abyssal Plain cannot be distinguished from those of other basin plains that exhibit a Poisson
1195 distribution. The results also indicate that the Iberian Abyssal Plain also has a different distribution of
1196 recurrence intervals from levee core JC27-46, suggesting a different long-term control on recurrence.

48

1197

1198

48

Figure 1

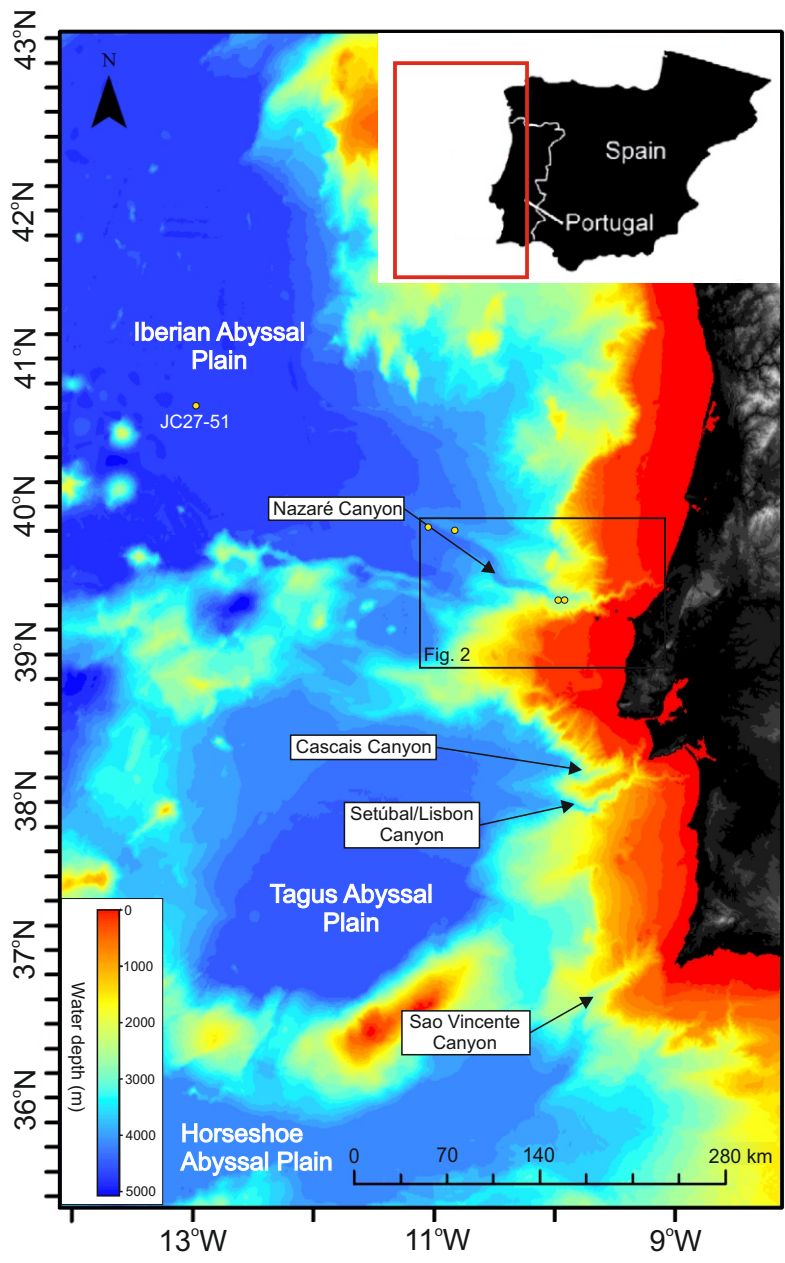


Figure 2

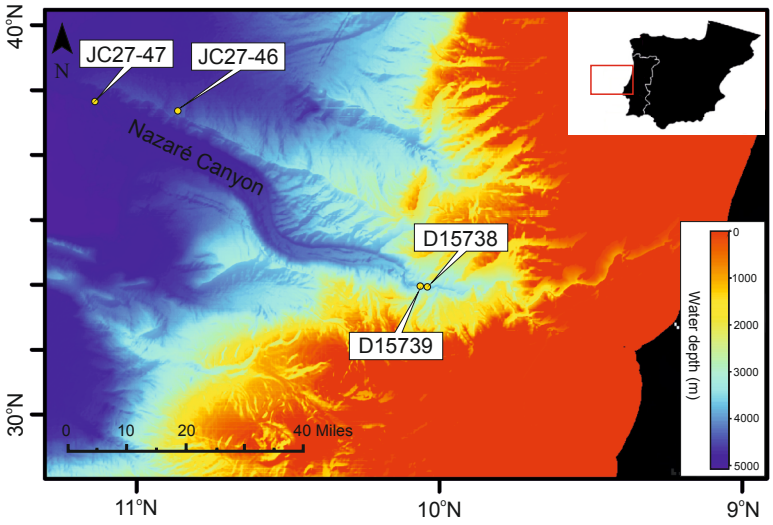


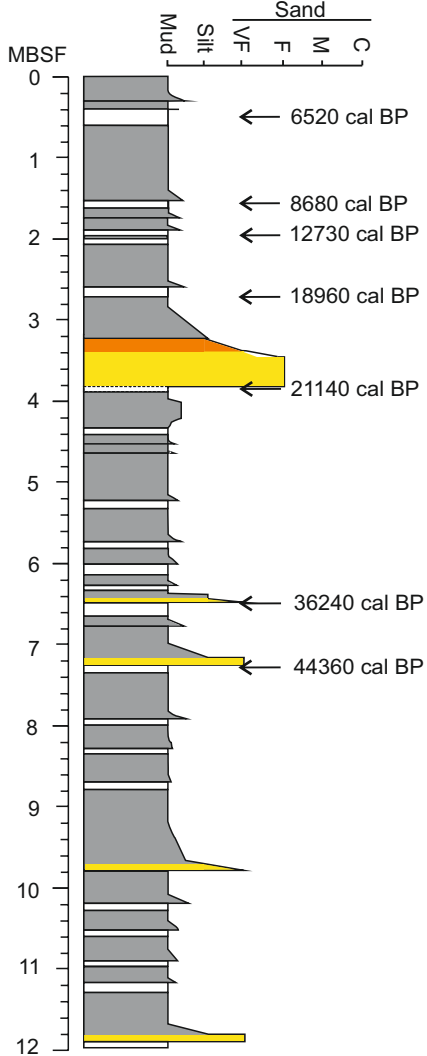
Figure 3

Abbyssal Plain

Northern canyon levee

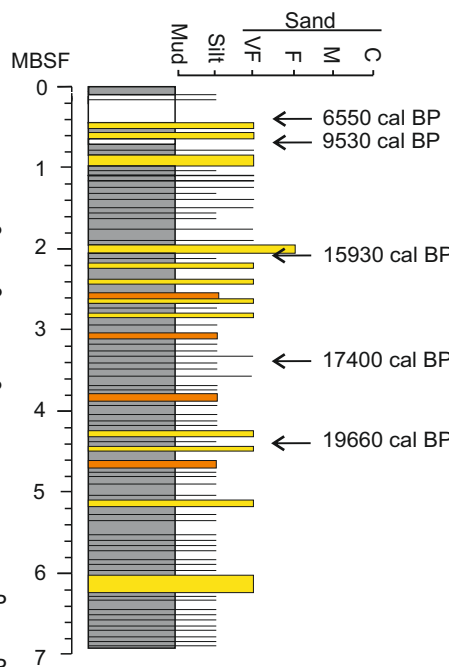
Intra-canyon terraces

JC27-51



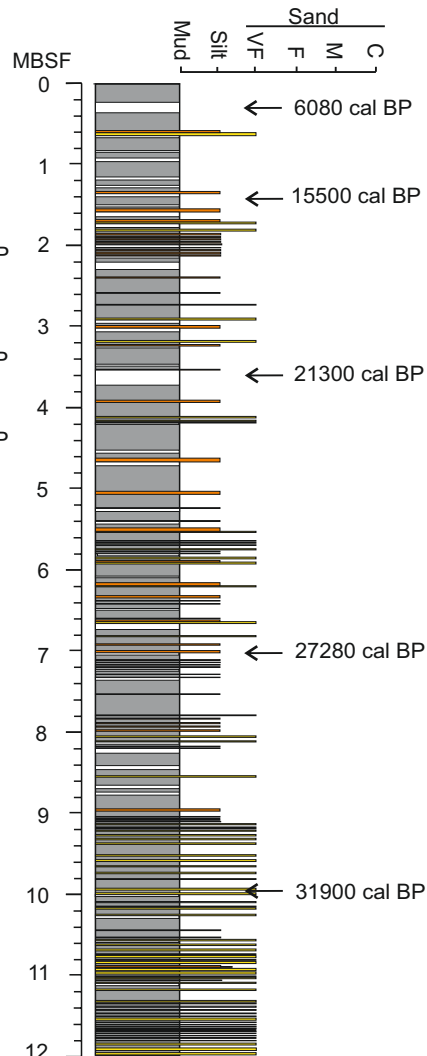
5350 m depth

JC27-47



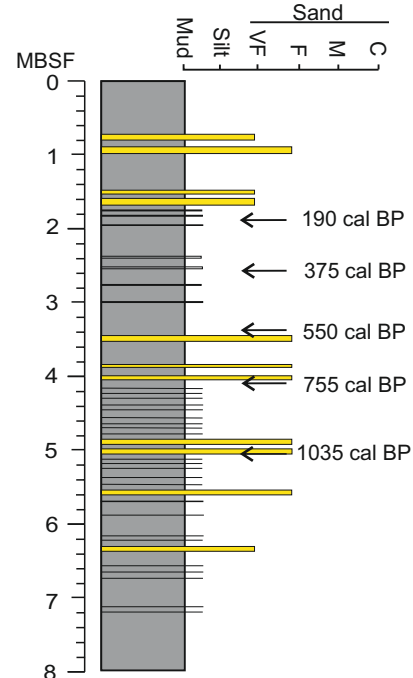
5060 m depth
50-100 m high on levee

JC27-46



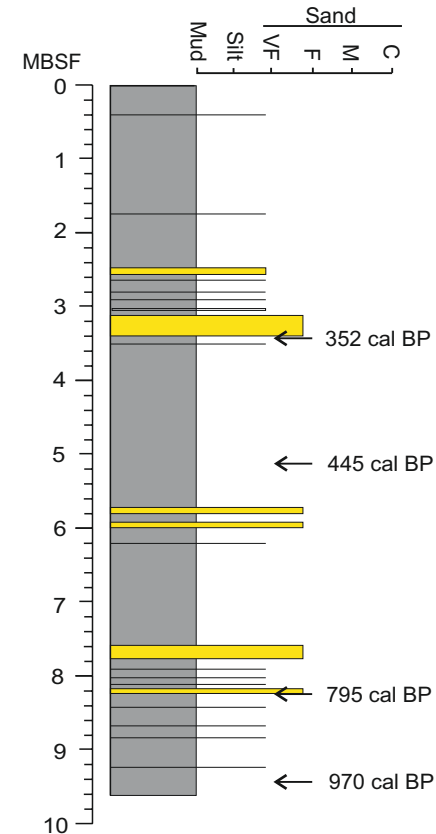
4750 m depth
150-200 m high on levee

D15738



3541 m depth
40 m high terrace

D15739



3432 m depth
40-60 m high terrace

Key:

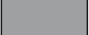





- | | | | |
|---|----------------|---|---------------------|
|  | Turbidite mud |  | Hemipelagite |
|  | Turbidite sand |  | Thin turbidite base |
|  | Turbidite silt |  | Erosional surface |

Figure 4

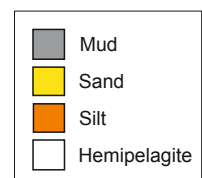
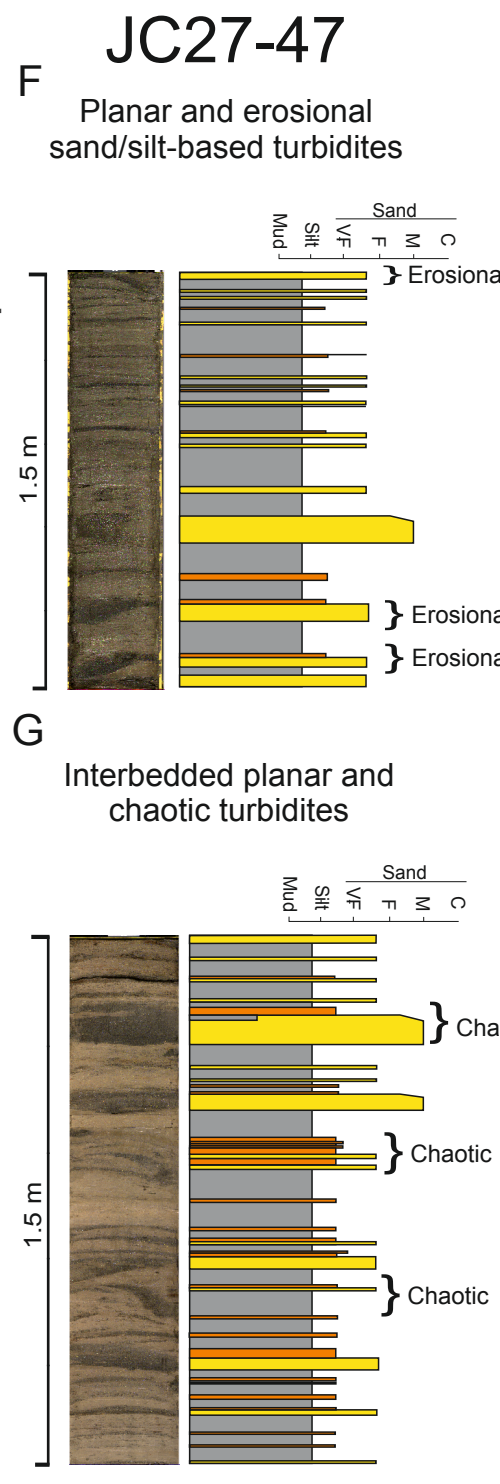
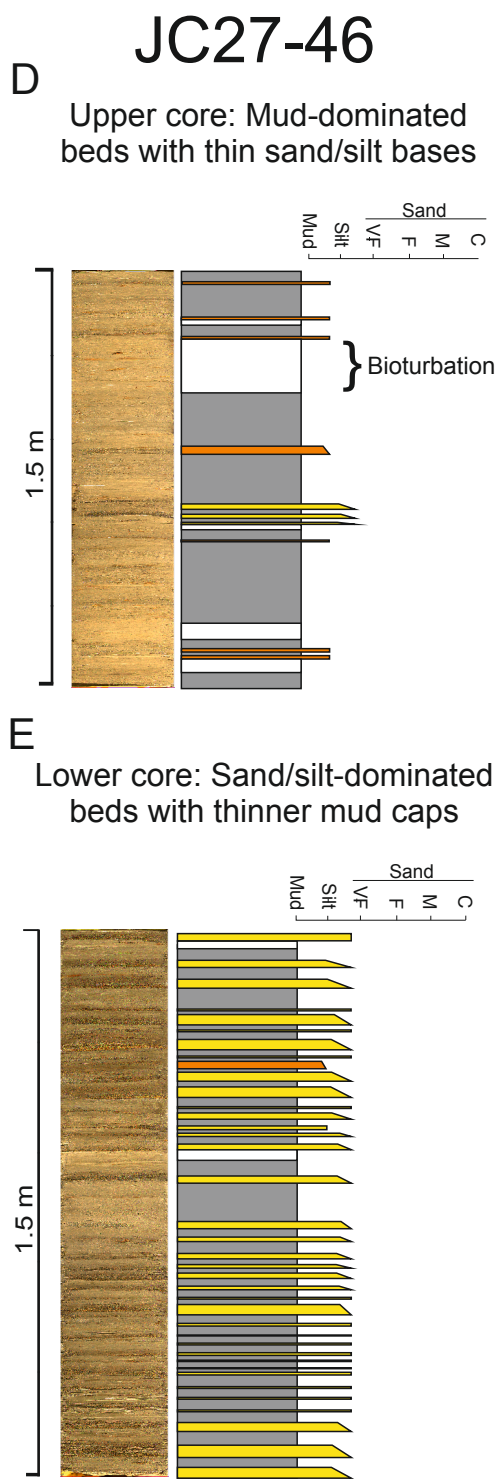
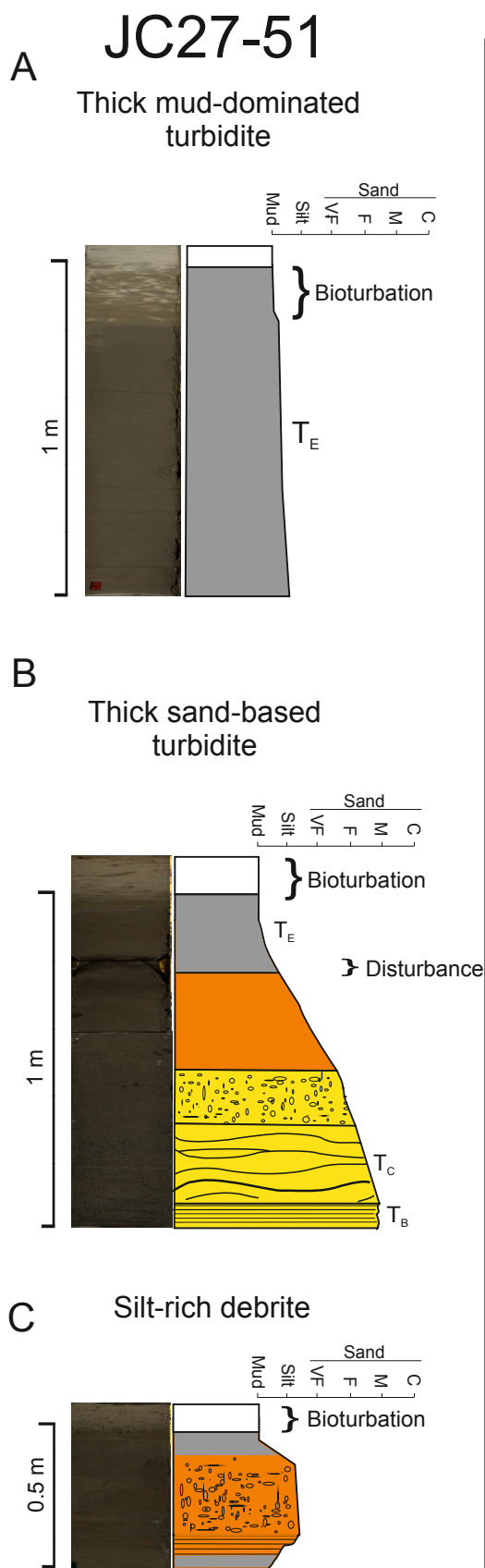


Figure 5
[Click here to download high resolution image](#)

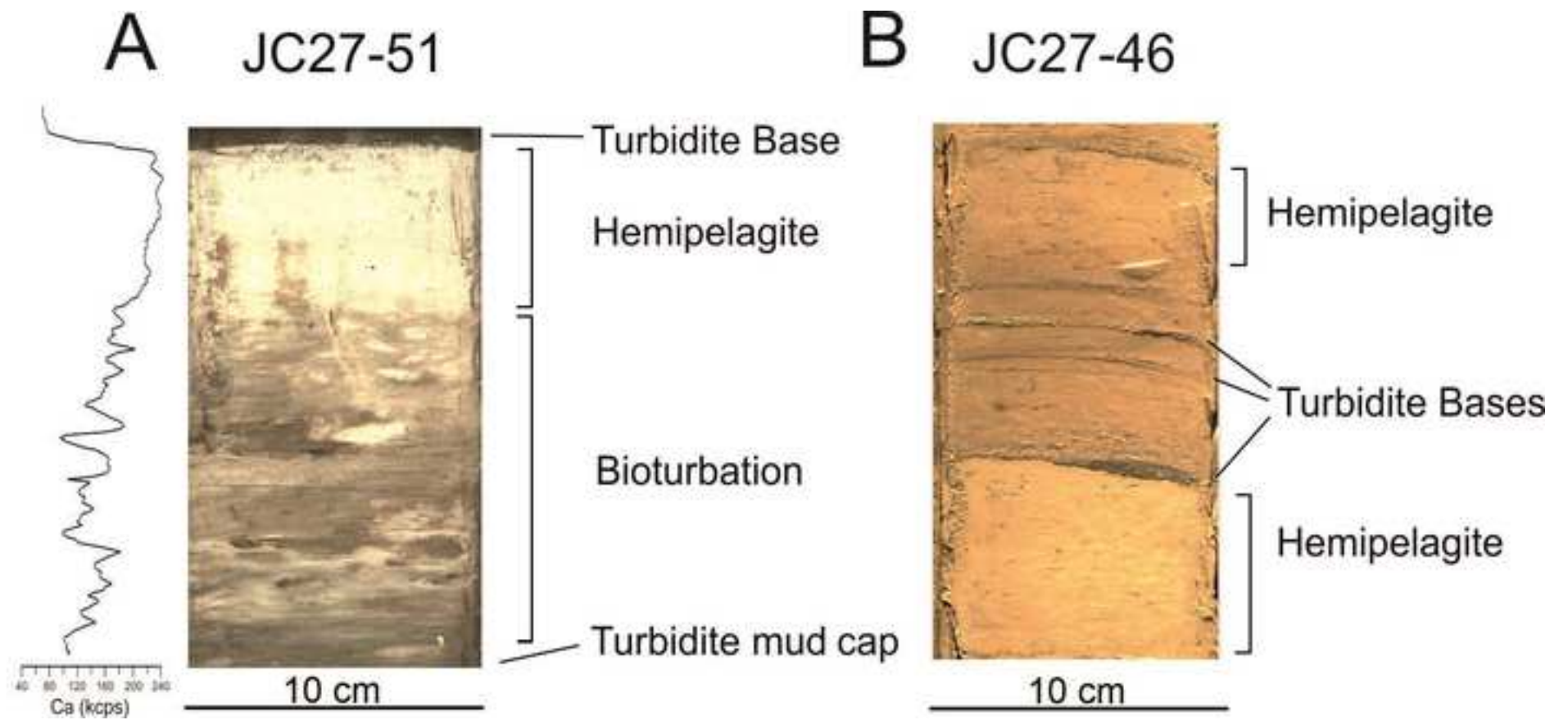


Figure 6

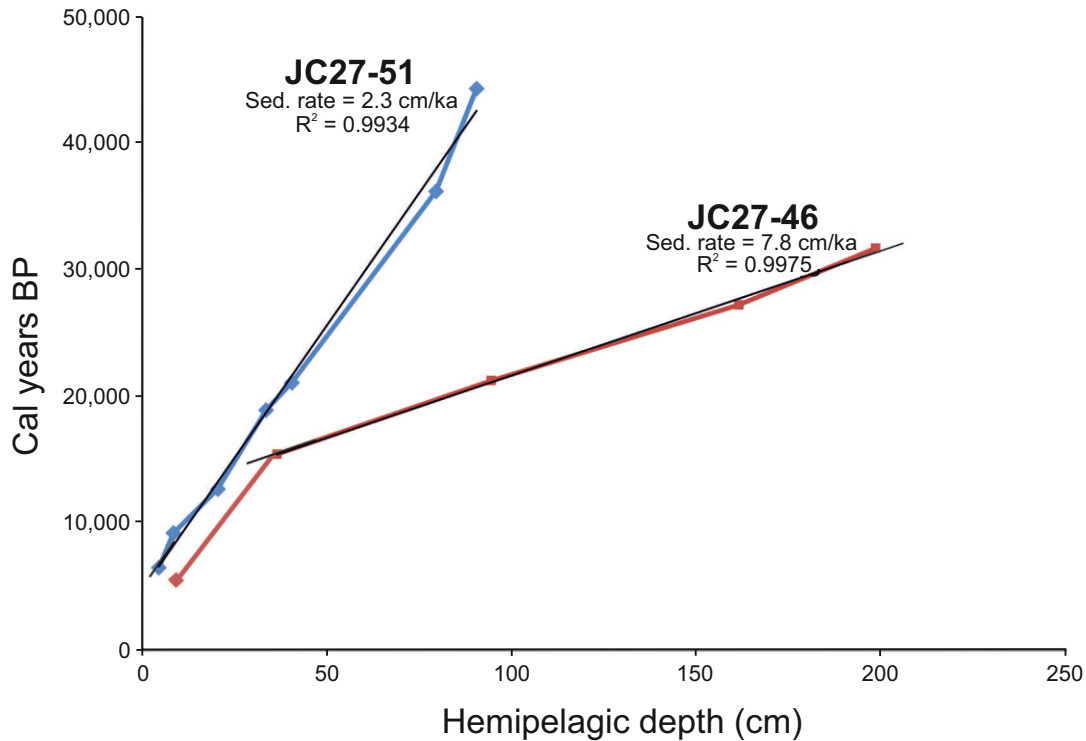
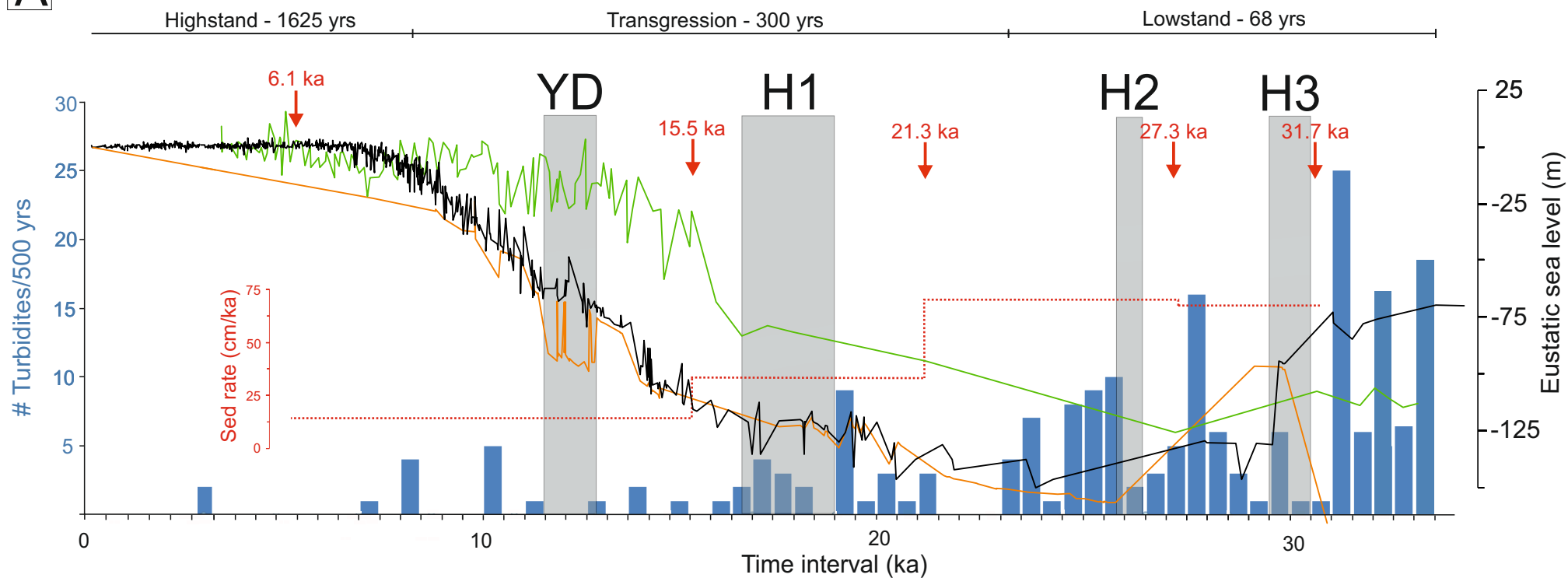


Figure 7

A

JC27-46 Average recurrence interval



B

JC27-47 Average recurrence interval

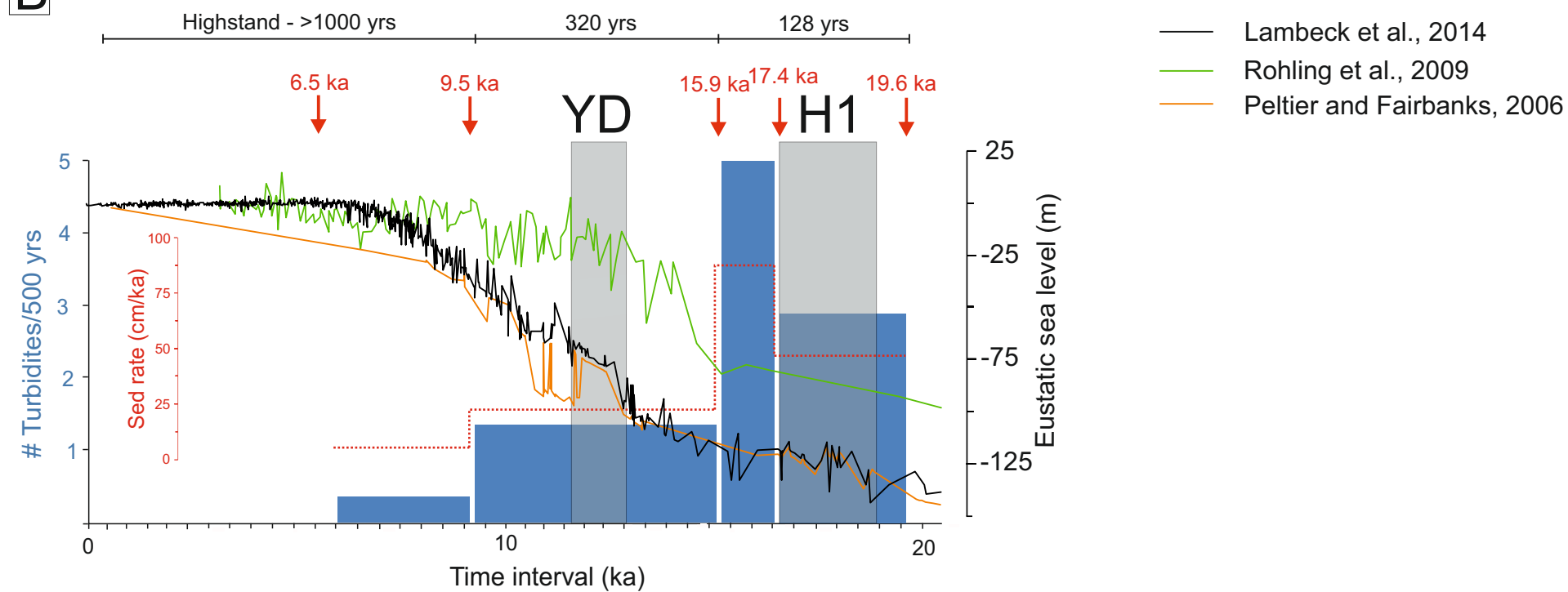
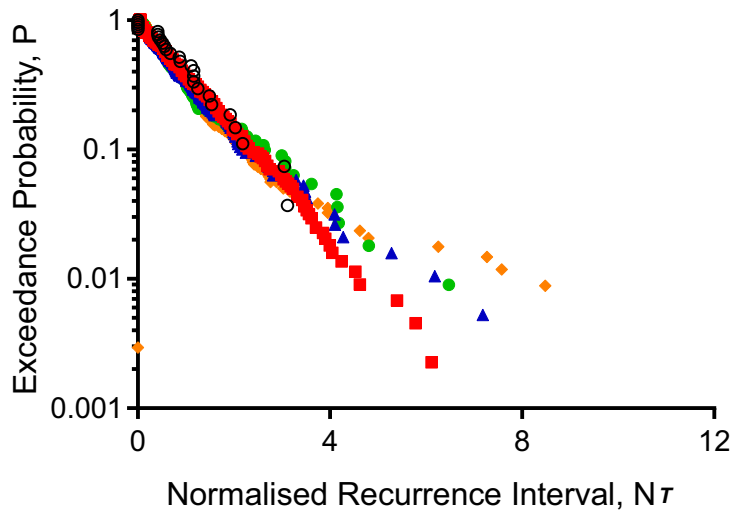
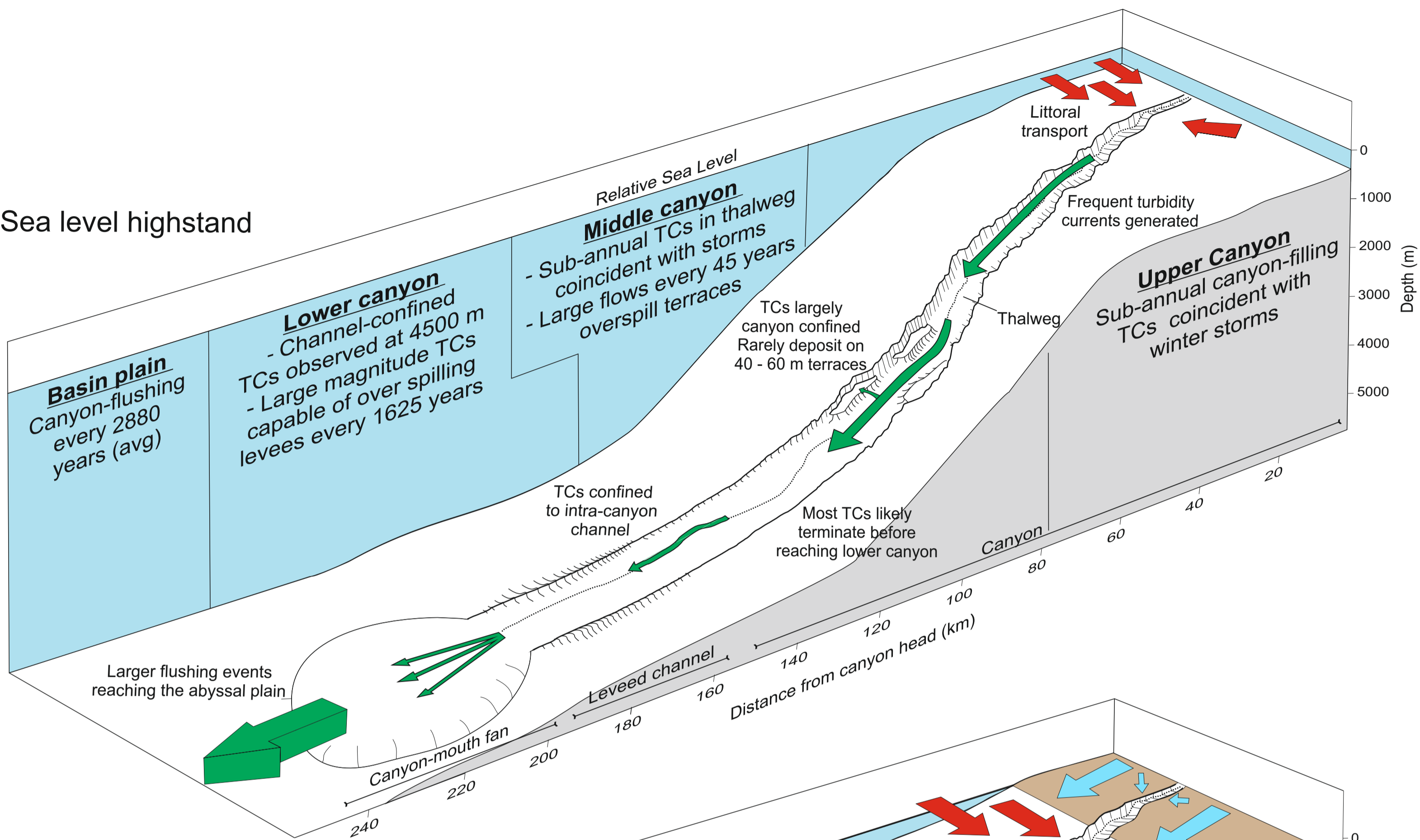


Figure 8

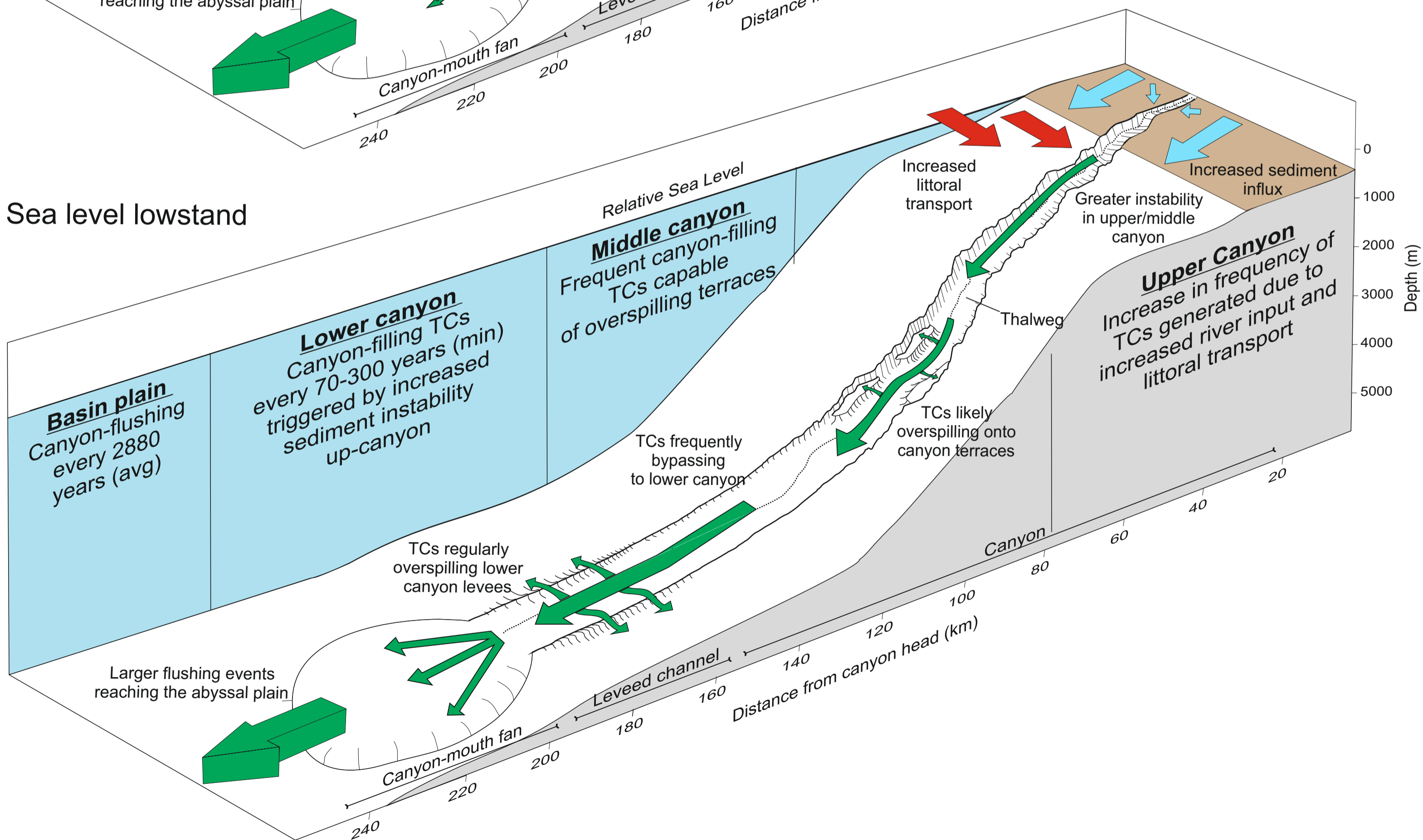


- Iberia Abyssal Plain [N=26]
- Marnoso-arenacea [N=696]
- ▲ Madeira Abyssal Plain [N=190]
- Southern Balearic Abyssal Plain [N=151]
- ◆ Zumaia Series [N=339]

A. Sea level highstand



B. Sea level lowstand



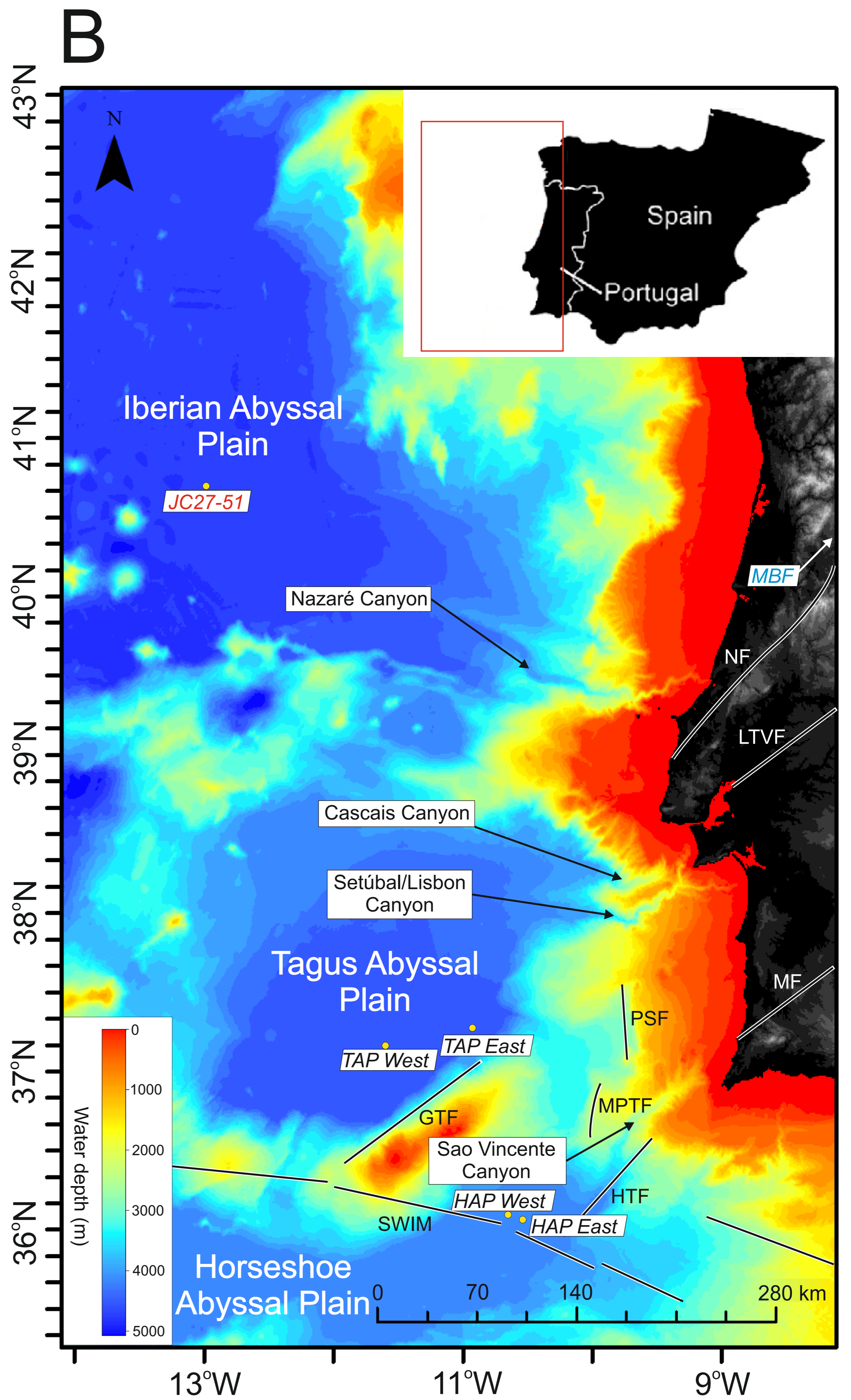
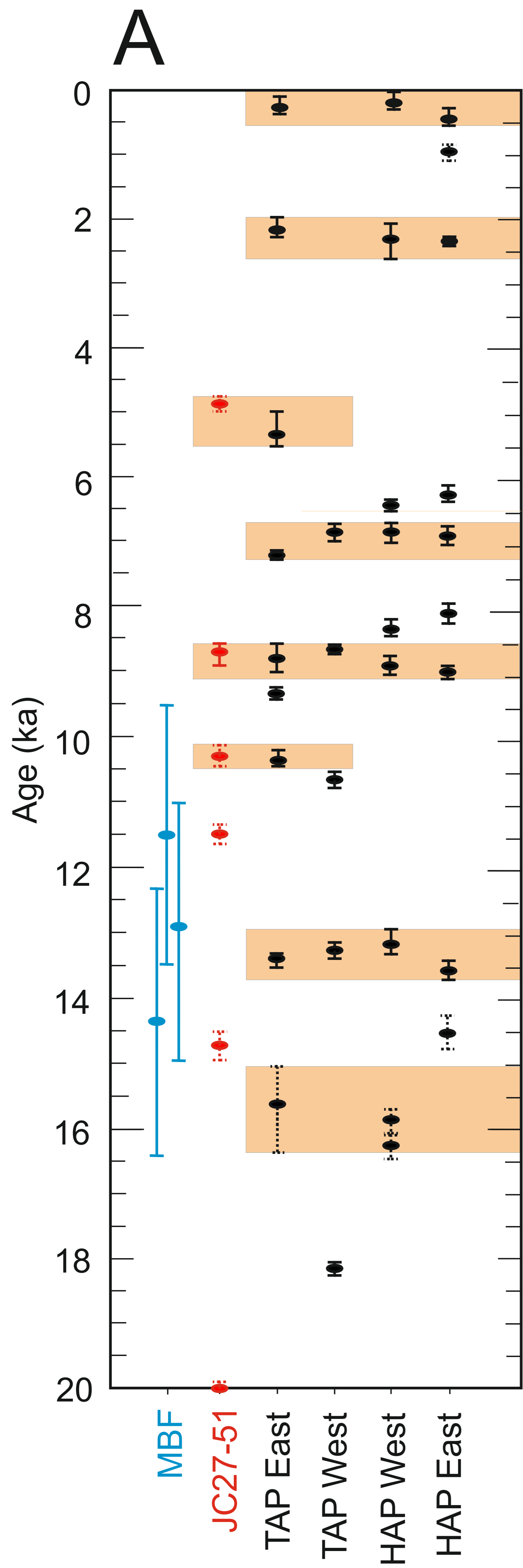


Table 1

[Click here to download Table: Table 1.xlsx](#)

Lab code	Core #	Core depth (cm)	Conventional age (BP)	Max. probability (Cal BP)	1 σ Cal age ranges (Cal BP)	2 σ Cal age ranges (Cal BP)
BETA-385402	JC27-46	32-33	5,940 \pm 30	6,078	5,995-6,165	5,918-6,233
BETA_385403	JC27-46	158-159	13,639 \pm 50	15,494	15,334-15,629	15,234-15,768
BETA_385404	JC27-46	349-350	18,290 \pm 60	21,303	21,143-21,465	20,994-21,599
BETA_385405	JC27-46	701-702	23,600 \pm 100	27,280	27,163-27,406	27,020-27,514
BETA_385406	JC27-46	996-997	28,790 \pm 140	31,750	31,568-32,146	31,449-32,521
SUERC-31798	JC27-47	53-54	6,120 \pm 35	6,270	6,197-6,341	6,117-6,422
BETA-401321	JC27-47	70.5-71.5	8,510 \pm 30	8,760	8,652-8,889	8,584-8,972
SUERC-31799	JC27-47	212-214	13,530 \pm 47	15,300	15,201-15,479	15,117-15,638
BETA-401322	JC27-47	340-341.5	14,910 \pm 50	14,700	17,211-17,469	17,089-17,576
SUERC-31802	JC27-47	445-448	16,910 \pm 55	19,580	19,484-19,725	19,360-19,894
	JC27-51	48.5-49.5	6,355 \pm 37	6,520	6,433-6,604	6,342-6,680
BETA-382057	JC27-51	155-156	8,470 \pm 30	8,680	8,604-8,769	8,567-8,893
	JC27-51	196.5-197.5	11,535 \pm 39	12,730	12,661-12,810	12,613-12,904
	JC27-51	264-265	16,415 \pm 53	18,960	18,883-19,083	18,808-19,206
	JC27-51	381-382	18,196 \pm 62	21,140	21,019-21,322	20,886-21,469
BETA-382053	JC27-51	649-650	33,010 \pm 200	36,240	36,000-36,454	35,722-36,719
BETA-382054	JC27-51	726-727	41,500 \pm 550	44,360	43,825-44,875	43,310-45,314
SUERC-18143	D15738	178.5	573 \pm 37	190		90-290
SUERC_18146	D15738	250.5	738 \pm 37	375		290-460
SUERC_18147	D15738	335	934 \pm 37	550		480-620
SUERC_18148	D15738	405	1,204 \pm 37	755		660-850
SUERC_18149	D15738	509.5	1,482 \pm 35	1,035		940-1,130
SUERC-18150	D15739	334.5	703 \pm 37	352		270-435
SUERC-18151	D15739	489.5	821 \pm 37	445		370-520
SUERC-18153	D15739	829.5	1,245 \pm 37	795		700-890
SUERC-18156	D15739	959.5	1,411 \pm 37	970		890-1,050

Table 2

[Click here to download Table: Table 2.xlsx](#)

Turbidite no	Turbidite base depth (cm)	Turbidite thickness (cm)	Approx age (cal BP)	Recurrence interval (years)
1	25	25	4,850	0
2	45	20	4,850	4,430
3	155	103	8,680	1,700
4	172	13	10,300	0
5	187	15	10,300	1,200
6	194	4	11,505	3,200
7	254	53	14,700	5,550
8	378	110	20,250	1,350
9	428	46	21,600	1,500
10	454	22	23,100	0
11	468	14	23,100	0
12	503	35	23,100	1,600
13	523	16	24,700	2,550
14	570	40.5	27,250	1,950
15	597	24	29,200	4,300
16	618	10	33,500	1,200
17	645	24	34,700	9,000
18	671	12.5	43,700	0
19	725	54	43,700	3,600
20	790.5	57.5	47,300	5,850
21	837	36	53,150	1,250
22	870	30.5	54,400	8,800
23	978	102	63,200	3,350
24	1016	38	66,550	3,350
25	1050	26	69,900	6,300
26	1091	36	76,200	2,500
27	1119	20	78,700	3,350
28	1187	60	82,050	

Avg: 2800

Supplementary table 1

[Click here to download Supplementary Materials: Supplementary table 1.xlsx](#)

Supplementary table 2

[Click here to download Supplementary Materials: Supplementary table 2.xlsx](#)

Supplementary table 3

[Click here to download Supplementary Materials: Supplementary table 3.xlsx](#)